The Astrophysical Journal, 761:139 (24pp), 2012 December 20 doi:10.1088/0004-637X/761/2/139

A POPULATION OF $z > 2$ FAR-INFRARED *HERSCHEL*-SPIRE-SELECTED STARBURSTS

C. M. Casey[1], S. Berta[2], M. Béthermin[3,4], J. Bock[5,6], C. Bridge[5], D. Burgarella[7], E. Chapin[8,9], S. C. Chapman[10,11], D. L. Clements[12], A. Conley[13], C. J. Conselice[14], A. Cooray[5,15], D. Farrah[16], E. Hatziminaoglou[17], R. J. Ivison[18,19], E. le Floc'h[3], D. Lutz[2], G. Magdis[3,20], B. Magnelli[2], S. J. Oliver[21], M. J. Page[22], F. Pozzi[23], D. Rigopoulou[20,24], L. Riguccini[3,25], I. G. Roseboom[19,21], D. B. Sanders[1], Douglas Scott[8], N. Seymour[22,26], I. Valtchanov[9], J. D. Vieira[5], M. Viero[5], and J. Wardlow[15]

[1] Institute for Astronomy, University of Hawaii, 2680 Woodlawn Drive, Honolulu, HI 96822, USA
[2] Max-Planck-Institut für Extraterrestrische Physik, Giessenbachstrasse, D-85748 Garching, Germany
[3] Laboratoire AIM-Paris-Saclay, CEA/DSM/Irfu-CNRS-Université Paris Diderot, CE-Saclay, pt courrier 131, F-91191 Gif-sur-Yvette, France
[4] Institut d'Astrophysique Spatiale (IAS), bâtiment 121, Université Paris-Sud 11 and CNRS (UMR 8617), F-91405 Orsay, France
[5] Cahill Center for Astronomy and Astrophysics, California Institute of Technology, 1200 E. California Blvd., Pasadena, CA 91125, USA
[6] Jet Propulsion Laboratory, 4800 Oak Grove Drive, Pasadena, CA 91109, USA
[7] Laboratoire d'Astrophysique de Marseille (LAM), Université d'Aix-Marseille & CNRS, UMR7326, 38 rue F. Joliot-Curie, F-13388 Marseille Cedex 13, France
[8] Department of Physics & Astronomy, University of British Columbia, 6224 Agricultural Road, Vancouver, BC V6T 1Z1, Canada
[9] European Space Astronomy Centre, Villanueva de la Cañada, E-28691 Madrid, Spain
[10] Institute of Astronomy, University of Cambridge, Madingley Road, Cambridge CB3 0HA, UK
[11] Department of Physics and Atmospheric Science, Dalhousie University, 6310 Coburg Rd, Halifax, NS B3H 4R2, Canada
[12] Astrophysics Group, Imperial College London, Blackett Laboratory, Prince Consort Road, London SW7 2AZ, UK
[13] Center for Astrophysics and Space Astronomy 389-UCB, University of Colorado, Boulder, CO 80309, USA
[14] School of Physics and Astronomy, University of Nottingham, Nottingham NG7 2RD, UK
[15] Department of Physics & Astronomy, University of California, Irvine, CA 92697, USA
[16] Department of Physics, Virginia Tech, Blacksburg, VA 24061, USA
[17] ESO, Karl-Schwarzschild-Str. 2, D-85748 Garching bei München, Germany
[18] UK Astronomy Technology Centre, Royal Observatory, Blackford Hill, Edinburgh EH9 3HJ, UK
[19] Institute for Astronomy, University of Edinburgh, Royal Observatory, Blackford Hill, Edinburgh EH9 3HJ, UK
[20] Department of Astrophysics, Denys Wilkinson Building, University of Oxford, Keble Road, Oxford OX1 3RH, UK
[21] Astronomy Centre, Department of Physics & Astronomy, University of Sussex, Brighton BN1 9QH, UK
[22] Mullard Space Science Laboratory, University College London, Holmbury St. Mary, Dorking, Surrey RH5 6NT, UK
[23] Dipartimento di Fisica e Astronomia, Viale Berti Pichat, 6/2, I-40127 Bologna, Italy
[24] RAL Space, Rutherford Appleton Laboratory, Chilton, Didcot, Oxfordshire OX11 0QX, UK
[25] NASA Ames, Moffett Field, CA 94035, USA
[26] CSIRO Astronomy & Space Science, P.O. Box 76, Epping, NSW 1710, Australia
Received 2012 July 20; accepted 2012 October 12; published 2012 December 4

ABSTRACT

We present spectroscopic observations for a sample of 36 *Herschel*-SPIRE 250–500 μm selected galaxies (HSGs) at $2 < z < 5$ from the *Herschel* Multi-tiered Extragalactic Survey. Redshifts are confirmed as part of a large redshift survey of *Herschel*-SPIRE-selected sources covering $\sim$0.93 deg^2 in six extragalactic legacy fields. Observations were taken with the Keck I Low Resolution Imaging Spectrometer and the Keck II DEep Imaging Multi-Object Spectrograph. Precise astrometry, needed for spectroscopic follow-up, is determined by identification of counterparts at 24 μm or 1.4 GHz using a cross-identification likelihood matching method. Individual source luminosities range from $\log(L_{\rm IR}/L_\odot) = 12.5$–$13.6$ (corresponding to star formation rates (SFRs) 500–9000 $M_\odot$ yr^{-1}, assuming a Salpeter initial mass function), constituting some of the most intrinsically luminous, distant infrared galaxies discovered thus far. We present both individual and composite rest-frame ultraviolet spectra and infrared spectral energy distributions. The selection of these HSGs is reproducible and well characterized across large areas of the sky in contrast to most $z > 2$ HyLIRGs in the literature, which are detected serendipitously or via tailored surveys searching only for high-z HyLIRGs; therefore, we can place *lower limits* on the contribution of HSGs to the cosmic star formation rate density (SFRD) at $(7 \pm 2) \times 10^{-3}$ $M_\odot$ yr^{-1} h^3 Mpc^{-3} at $z \sim 2.5$, which is $>$10% of the estimated total SFRD of the universe from optical surveys. The contribution at $z \sim 4$ has a lower limit of 3×10^{-3} $M_\odot$ yr^{-1} h^3 Mpc^{-3}, $\gtrsim$20% of the estimated total SFRD. This highlights the importance of extremely infrared-luminous galaxies with high SFRs to the buildup of stellar mass, even at the earliest epochs.

Key words: galaxies: evolution – galaxies: high-redshift – galaxies: starburst – infrared: galaxies – submillimeter: galaxies

Online-only material: color figures

1. INTRODUCTION

Submillimeter galaxies (SMGs, often selected by 850 μm–1 mm flux densities $\gtrsim$2 mJy; Smail et al. 1997; Hughes et al. 1998; Barger et al. 1998; Eales et al. 1999) are the most intrinsically luminous starburst galaxies that have been identified to date. SMGs are thought to evolve much like local ultraluminous infrared galaxies (ULIRGs; Sanders et al. 1988; Sanders & Mirabel 1996) via major mergers. The "merger" evolutionary scenario starts with the collision of gas-rich disk galaxies igniting an intense, short-lived ($\tau \sim 100$ Myr) phase of gas consumption and dust production via a starburst, followed by the formation of a quasar and eventually (1–2 Gyr later) a massive, elliptical galaxy. In contrast to local ULIRGs, SMGs at $z \sim$ 2–3 are much more luminous and more massive (in $M_\star$ and $M_{\rm H_2}$), and sometimes much larger (Chapman et al. 2004b;

Biggs & Ivison 2008), thus they have been dubbed "scaled-up" (Tacconi et al. 2008), providing evidence for cosmic downsizing (Cowie et al. 1996).

The observation that the most luminous infrared sources are at the highest redshifts (e.g., GN20; Daddi et al. 2009) poses a unique problem for galaxy evolution studies. How can these distant ULIRGs be formed so quickly after the big bang with such high star formation rates (SFRs)? Their extreme infrared luminosities might stem from different evolutionary histories than the local ULIRG mergers, i.e., secular gas accretion (Dekel et al. 2009; Davé et al. 2010), but solving the origin of infrared-luminous galaxies requires large, uniformly selected samples of ULIRGs across many epochs.

Unfortunately, most $z > 2$ infrared-luminous galaxy samples number ∼30 galaxies selected in non-uniform, biased ways. It is well known that the selection of SMGs is severely biased, first against galaxies with warmer dust temperatures (Blain et al. 2004; Chapman et al. 2004a, 2010; Casey et al. 2009, 2011a; Magdis et al. 2010) and second, against galaxies at higher redshifts since they are unlikely to have bright radio counterparts (Chapman et al. 2005) or 24 μm counterparts (Ivison et al. 2007; Clements et al. 2008) due to the radio K-correction and surface brightness dimming. Third, SMGs at $z > 2$ are often detected in inhomogeneous, serendipitous studies with a range of detection thresholds at different wavelengths in the far-infrared. Fourth, the spectroscopic follow-up and redshift confirmation of these sources are non-uniform; their success rate could relate to their FIR properties, e.g., color or single-band flux density. The lack of SMGs with confirmed redshifts $z \gtrsim 3.5$ has been alleviated in recent years with the discovery of several systems at $4 < z < 5.3$ (Wang et al. 2007, 2009; Daddi et al. 2009; Coppin et al. 2009; Capak et al. 2011; Smolčić et al. 2011; Walter et al. 2012); however, this work has been severely limited by the rarity of $z > 3.5$ sources and the small area, non-uniform coverage of existing ground-based submillimeter surveys with SCUBA, MAMBO, LABOCA, and AzTEC.

The *Herschel Space Observatory*[27] (Pilbratt et al. 2010) has surveyed ∼200 deg^2 down to the ≈ 5 mJy confusion limit of Spire (Griffin et al. 2010; Nguyen et al. 2010) as part of the *Herschel* Multi-tiered Extragalactic Survey (HerMES; Oliver et al. 2012) at 250, 350, and 500 μm. Although high-z infrared galaxies are spatially rare, SPIRE has mapped much larger sky areas than previous submillimeter surveys and thus can detect a statistically significant population of $z > 2$ starbursts with a well-characterized selection.

This paper presents redshifts and spectra for 36 $2 < z < 5$ *Herschel*-Spire-selected galaxies (HSGs) identified within a large sample of ≈1600 Spire-selected galaxies spectroscopically surveyed over ∼1 deg^2. In Section 2, we describe the source selection, biases in 24 μm and radio samples, and spectroscopic observations. In Section 3, we present redshift identifications. In Section 4, we present our results, from derived luminosities, dust temperatures, the FIR/radio correlation, to composite rest-frame ultraviolet and infrared spectra. In Section 5, we discuss the context of our results by calculating the HSG contribution to the cosmic star formation rate density (SFRD) and the implications for infrared-luminous galaxy evolution in the early universe. In Section 6, we conclude. Throughout we use a flat ΛCDM cosmology (Hinshaw et al. 2009) with $H_0 = 71$ km s^{-1} Mpc^{-1} and $\Omega_M = 0.27$. When possible, we discuss distance and volume using the general unit, h^{-1} Mpc.

[27] *Herschel* is an ESA space observatory with science instruments provided by European-led Principal Investigator consortia and with important participation from NASA.

2. SAMPLE AND OBSERVATIONS

2.1. The Herschel-SPIRE-selected Galaxy (HSG) Sample

The sources described in this paper were detected by the Spire instrument (Griffin et al. 2010) on board the *Herschel Space Observatory* as part of the HerMES (Oliver et al. 2012). Sources were spectroscopically observed in a large redshift survey follow-up program described in detail in a companion paper, Casey et al. (2012), hereafter C12. The results of the redshift survey have been split between two papers due to the significant differences in the comprehensive 731 source $z < 2$ sample, identified through [O II], [O III], Hβ, and Hα emission, than the 36 galaxies at $z > 2$ identified primarily through rest-frame ultraviolet features. We refer the reader to C12 for a detailed discussion of our source selection and completeness and only briefly summarize those results here.

Due to the large beam size of Spire observations (18″, 25″, and 36″, respectively, at 250, 350, and 500 μm), counterpart identification and point source photometry are performed by extracting flux from Spire maps (Levenson et al. 2010) at known positions of *Spitzer*-MIPS 24 μm and Very Large Array 1.4 GHz sources (see C12 for more details on data). This cross-identification prior source extraction method (called "XID") is described in detail in Roseboom et al. (2010) and Roseboom et al. (2012). The disadvantage of the XID method is that it relies on Spire-bright sources being detectable at 24 μm and/or 1.4 GHz, an assumption that is known to sometimes fail at $z \gtrsim 3$, depending on the depth of 24 μm or 1.4 GHz coverage. For this reason, our spectroscopic survey was conducted in the HerMES coverage areas with the deepest available ancillary data in six different legacy fields: Lockman Hole North (LHN; $\alpha \sim$10h 46′, $\delta \sim$59°), Cosmic Evolution Survey field (COSMOS; $\delta \sim 10^h$ 0′, $\delta \sim 2°$), Great Observatories Origins Deep Survey North field (GOODS-N; $\alpha \sim 12^h$ 36′, $\delta \sim 62°$), Elais-N1 (EN1; $\alpha \sim 16^h$ 0′, $\delta \sim 54°$), the UKIDSS Ultra-deep field ($\alpha \sim 2^h$ 19′, $\delta \sim$–5°), and the Extended Chandra Deep Field South (CDFS; $\alpha \sim$ 3h 30′, $\delta \sim$–28°).

Sources were selected for spectroscopic follow-up by detection at $>3\sigma$ significance in at least one of the three Spire bands. The absolute flux limit changes field to field depending on XID prior source density, but averages ∼ 10–12 mJy across the three bands. Throughout the rest of this paper we refer to this population as HSGs for convenience. Higher priority follow-up is given to sources detected in all three bands, however the source density of all Spire-detected sources is low enough such that >98% of all HSGs can be surveyed within one spectroscopic mask area, whether it be with the Keck I Low Resolution Imaging Spectrometer (LRIS; covering 5.′5 × 7.′8) or with the Keck II DEep Imaging Multi-Object Spectrograph (DEIMOS; covering 5′ × 16.′7).

2.2. Biases in the HSG Sample

Although the completeness of the XID source identification technique is >95% for sources at $z < 2$ (Magdis et al. 2010; Roseboom et al. 2010, 2012; Béthermin et al. 2011), the completeness at higher redshifts is difficult to estimate since an increasing, non-negligible fraction of Spire-bright sources drop out at 24 μm and/or 1.4 GHz with increasing redshift. This is also a function of the 24 μm and 1.4 GHz depth, which is different field to field. Since this paper focuses exclusively on

the $z > 2$ SPIRE-bright population, it is important to emphasize that the sample here is incomplete, biased, and is not representative of all SPIRE-bright galaxies at $z > 2$. Constraining the whole SPIRE population at $z > 2$ will require detailed high-resolution submillimeter follow-up, e.g., from ALMA, of a large population of SPIRE-bright systems, particularly those that are radio and 24 μm faint and for sources that fail to yield optical spectroscopic identifications.

Note that the purity of the XID technique in counterpart identification is not guaranteed. In other words, XID might be incorrect in its identification of the multiwavelength counterpart for a *Herschel* source (as mentioned in Roseboom et al. 2010). The purity of this sample is impossible to gauge without direct far-infrared interferometric observations (this does away with confusion noise, as in Wang et al. 2011). However, we do note that radio counterpart identifications are more robust than 24 μm counterparts due to their source rarity and radio's direct scaling with FIR luminosity (Chapman et al. 2003, 2005). Half of our sample is radio identified, with the other half showing no overall bias or trends which would skew our results.

Another possible bias of the HSG sample is the method of spectroscopic targeting. Our Keck observations were centered around high-priority "red" SPIRE sources (e.g., $S_{250} < S_{350} < S_{500}$), which are thought to be the highest-redshift SPIRE sources (e.g., Cox et al. 2011). While only one to two "red" targets were chosen per mask, this could skew the total redshift distribution higher than if masks were laid down arbitrarily on the sky. As C12 describes, and as we discuss later in Section 5, we measure the impact of "red" sources on the overall redshift distribution to be negligible since many of the "red" targets failed to yield spectroscopic identifications.

2.3. Spectroscopic Observations

Spectroscopic observations were carried out at the W. M. Keck Observatory using the LRIS on Keck I and the DEIMOS on Keck II in 2011 and 2012. LRIS observations were carried out on 2011 February 6, 2012 January 26, 2012 January 27, and 2012 February 27 with the 400/3400 grism, 560 nm dichroic, and primarily the 400/8500 grating in the red with central multi-slit wavelength 8000 Å for the 5.′5 × 7.′8 mask. This setup yields a 1.09 Å dispersion in the blue ($R \sim 4000$) and 0.80 Å dispersion in the red ($R \sim 9000$). Integration times varied from ∼2700 to 5600 s per mask depending on air mass and weather. DEIMOS observations were carried out on 2011 May 28, 2011 May 29, 2011 November 28, 2012 February 16, and 2012 February 17. The 600 lines mm^{-1} grating and 7200 Å blaze angle were used, resulting in a 0.65 Å dispersion ($R \sim 11000$). The GG455 filter was used to block higher order light, and typical integration times per mask were ∼2700–4800 s. The resolution in LRIS red and DEIMOS is sufficient to distinguish between a single emission line (e.g., Lyα) and the [O II] doublet (rest-frame separation of 3 Å). Data reduction for LRIS was done using our own custom-built IDL routines, while we used the DEEP2 DEIMOS data reduction pipeline for DEIMOS data.[28]

Twenty-five LRIS masks were observed (thirteen under photometric conditions), and twenty-nine DEIMOS masks were observed (sixteen under photometric conditions), surveying a total of 1594 SPIRE-selected sources in 0.93 deg^2 (0.43 deg^2 observed in photometric conditions). Of 1594 sources surveyed, 767 have confirmed spectroscopic redshifts identified primarily by the [O II] doublet, [O III], Hβ, Hα, [N II], Ca H and Ca K absorption, the Balmer break, Hγ, Lyα, C IV, C III], He II, and the Lyman break. The lower redshift sources identified through rest-frame optical signatures are discussed in C12. Of the 767 confirmed redshifts, 36 are above $z = 2$ and thus comprise the HSG sample discussed in this paper. Out of the 36, we categorize 22 as secure based on the signal to noise (S/N) of Lyα and/or detection of multiple spectral features, discussed in the next section.

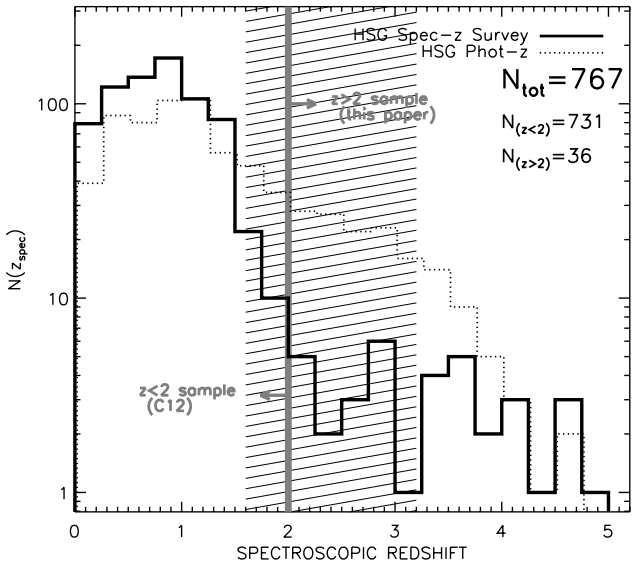

Figure 1. Redshift distribution of *Herschel*-SPIRE-selected galaxies from our survey. This paper analyzes the $z > 2$ sample, which consists of 36 sources, while the $z < 2$ sample, consisting of 731 sources, is analyzed in a companion paper (Casey et al. 2012 (C12)). The distribution of photometric redshifts comes from sources in the COSMOS field, where the quality of the photometric redshifts is high over a large area; this distribution includes sources not necessarily in the spectroscopic survey, but follows the same selection as spectroscopic targets. The hashed area from $1.6 < z < 3.2$ highlights the DEIMOS redshift range where there is a deficit of sources due to spectroscopic incompleteness.

Note that the 36 source sample discussed in this paper was not selected in any special way in SPIRE color, photometric redshift, or optical characteristics. There was no special selection imposed that would yield more high-redshift identifications, and the selection differs in no way from the lower redshift-confirmed sources. This paper is simply a description of all $z > 2$ sources confirmed in our large spectroscopic survey.

The DEIMOS wavelength coverage roughly spans 4500–9500 Å, whereas the LRIS coverage spans 3000–10000 Å. The limited wavelength coverage of DEIMOS results in a gap in our redshift coverage between $1.6 < z < 3.2$, which does not occur for LRIS observations. Indeed, very few sources observed by DEIMOS are identified in that redshift range, with the exception of 1HERMES X1.4 J104642.89+585650.0 at $z = 2.841$ and 1HERMES X24 J160545.99+534544.4 at $z = 2.555$. These are both quasars with strong, broad C IV emission. We take the DEIMOS redshift desert into account when calculating the luminosity function and contribution to the cosmic SFRD later in Section 5. The redshift distribution for all *Herschel*-SPIRE galaxies is shown in Figure 1. The photometric redshift distribution shown comes from all HSGs in the COSMOS field, not limited to those targeted for spectroscopic observations.

3. REDSHIFT IDENTIFICATION AND SPECTRA

Table 1 summarizes the spectroscopic identifications and multi-wavelength properties of the 36 SPIRE-selected galaxies

[28] The analysis pipeline used to reduce the DEIMOS data was developed at UC Berkeley by Michael Cooper with support from NSF grant AST-0071048.

Table 1
$z > 2$ Identified SPIRE-selected Galaxies

Name	z_{spec}	Comments	Class	z_{phot}	S_{24} (μJy)	S_{100} (mJy)	S_{160} (mJy)	S_{250} (mJy)	S_{350} (mJy)	S_{500} (mJy)	$S_{1.4GHz}$ (μJy)	L_{IR} ($L_\odot$)	T_{dust} (K)
1HERMES X24 J033136.96−275510.9...	3.145[L]	Lyα-break	LBG	3.44[d]	265 ± 11	...	...	15.5 ± 3.8	20.8 ± 3.8	24.0 ± 4.8	...	$(1.0^{+0.3}_{-0.2}) \times 10^{13}$	40.6 ± 3.6
1HERMES X1.4 J033151.94−275326.9...	2.938[L]	Lyα; Si IV	SB	2.96[d]	397 ± 14	...	...	12.9 ± 3.9	21.6 ± 3.7	24.2 ± 4.2	54.3 ± 12.8	$(1.2^{+0.3}_{-0.2}) \times 10^{13}$	43.8 ± 3.4
1HERMES X24 J033319.58−274119.7...	2.325[L]	Lyα	SB	1.84[d]	329 ± 13	...	...	16.0 ± 3.8	19.0 ± 3.8	15.2 ± 4.5	...	$(5.4^{+1.7}_{-1.3}) \times 10^{12}$	39.3 ± 3.8
1HERMES X24 J095830.24+015633.2...	2.327[L]	Diffuse Lyα	SB	1.70[a]	418 ± 16	...	...	19.2 ± 2.2	23.4 ± 3.0	23.0 ± 3.3	...	$(5.4^{+2.9}_{-1.9}) \times 10^{12}$	24.6 ± 3.7
1HERMES X24 J095916.08+021215.3...	4.454[L]	Lyα	SB	2.97[a]	282 ± 14	...	10.1 ± 3.4	25.8 ± 2.2	24.1 ± 2.9	14.7 ± 3.2	...	$(1.9^{+1.3}_{-0.7}) \times 10^{13}$	45.9 ± 10.7
1HERMES X24 J095917.28+021300.4...	2.101[L]	Lyα; Si IV; C IV;+	SB	1.95[a]	472 ± 17	...	8.4 ± 2.7	14.2 ± 2.2	14.7 ± 2.7	7.1 ± 3.0	...	$(4.4^{+1.4}_{-1.0}) \times 10^{12}$	51.5 ± 5.2
1HERMES X1.4 J095934.08+021706.3...	2.926[L]	Lyα	SB	2.94[a]	1451 ± 16	...	11.5 ± 2.9	11.4 ± 2.2	12.9 ± 3.4	0.2 ± 4.7	170 ± 15	$(2.0^{+0.4}_{-0.2}) \times 10^{13}$	100 ± 3.0
1HERMES X24 J095948.00+024140.7...	2.600[L]	Lyα; C IV	SB+AGN	2.27[a]	909 ± 16	...	13.6 ± 4.2	10.5 ± 2.2	10.7 ± 2.8	6.4 ± 3.0	...	$(5.9^{+5.3}_{-2.7}) \times 10^{12}$	39.4 ± 12.2
1HERMES X1.4 J100008.64+022043.1...	2.888[L]	Lyα-break; C IV	LBG	2.18[a]	574 ± 14	...	...	16.5 ± 2.2	12.3 ± 2.9	9.4 ± 3.6	66 ± 12	$(7.9^{+6.0}_{-3.4}) \times 10^{12}$	31.4 ± 7.2
1HERMES X24 J100020.16+021725.2...	2.105[L]	Lyα; Si IV; C IV	QSO	1.45[a]	401 ± 16	...	...	20.0 ± 2.2	12.6 ± 3.5	22.3 ± 3.7	...	$(5.7^{+1.3}_{-1.0}) \times 10^{12}$	32.9 ± 2.2
1HERMES X1.4 J100024.00+021210.9...	3.553[L]	Lyα; Si IV; C IV	SB+AGN	2.97[a]	175 ± 50	6.1 ± 1.5	31.7 ± 3.6	28.5 ± 2.7	28.8 ± 3.5	15.1 ± 5.7	84 ± 13	$(2.0^{+0.4}_{-0.3}) \times 10^{13}$	54.0 ± 5.3
1HERMES X24 J100036.00+021127.6...	2.103[L]	Lyα; Si IV; C IV	SB	1.48[a]	158 ± 17	...	11.2 ± 2.9	13.2 ± 2.7	21.2 ± 3.6	4.9 ± 11.4	...	$(2.7^{+1.3}_{-0.9}) \times 10^{12}$	29.0 ± 3.9
1HERMES X1.4 J100111.52+022841.3...	3.975[L]	Lyα-break; C IV	LBG	2.60[a]	201 ± 41	...	...	24.5 ± 2.2	32.9 ± 4.3	22.8 ± 6.8	59 ± 11	$(1.8^{+0.6}_{-0.5}) \times 10^{13}$	46.7 ± 7.2
1HERMES X24 J100133.36+023726.9...	2.619[L]	Diffuse Lyα†	SB	−99[a]	245 ± 15	...	...	10.1 ± 2.2	9.1 ± 2.9	0.0 ± 9.9	...	$(4.4^{+2.5}_{-1.6}) \times 10^{12}$	51.9 ± 8.3
1HERMES X24 J100146.56+024035.6...	2.050[L]	Si IV; C IV; He II	SB+AGN	1.88[a]	722 ± 17	4.5 ± 1.2	...	11.7 ± 2.2	6.9 ± 2.8	2.2 ± 3.1	...	$(4.7^{+1.8}_{-1.3}) \times 10^{12}$	70.7 ± 8.3
1HERMES X24 J100150.16+024017.2...	2.883[L]	Lyα	SB	2.57[a]	315 ± 19	...	17.5 ± 4.6	13.8 ± 2.2	12.2 ± 2.9	8.9 ± 4.0	...	$(7.1^{+6.2}_{-3.3}) \times 10^{12}$	48.4 ± 16.5
1HERMES X24 J100151.60+023909.5...	4.538[L]	Lyα†	SB	2.20[a]	433 ± 102	...	...	17.8 ± 2.2	0.5 ± 5.4	22.1 ± 3.2	...	$(1.7^{+2.3}_{-0.9}) \times 10^{13}$	35.0 ± 11.3
1HERMES X1.4 J104557.12+590000.4...	3.382[L]	Lyα; C IV	SB	3.38[c]	713 ± 7	5.7 ± 2.7	8.5 ± 4.8	16.9 ± 3.6	7.6 ± 3.9	0.0 ± 4.7	101.9 ± 15.9	$(1.7^{+0.5}_{-0.4}) \times 10^{13}$	87.6 ± 8.9
1HERMES X1.4 J104620.40+585933.4...	2.211[L]	Lyα; C IV	SB+AGN	2.12[c]	559 ± 7	...	...	13.1 ± 3.5	3.4 ± 3.9	0.0 ± 4.7	64.5 ± 11.8	$(5.1^{+2.7}_{-1.8}) \times 10^{12}$	63.1 ± 9.7
1HERMES X1.4 J104636.00+585650.0...	2.841[D]	C IV	QSO	1.84[c]	166 ± 7	...	...	11.3 ± 3.5	5.4 ± 4.0	0.0 ± 4.9	19.4 ± 3.6	$(4.1^{+3.8}_{-2.0}) \times 10^{12}$	48.0 ± 10.8
1HERMES X24 J104642.89+585532.8...	3.626[D]	Lyα; C IV	SB+AGN	−99[c]	221 ± 7	...	...	9.5 ± 3.5	14.1 ± 4.0	0.0 ± 8.4	...	$(9.1^{+3.7}_{-2.6}) \times 10^{12}$	62.1 ± 7.4
1HERMES X1.4 J104649.92+590039.6...	4.710[L]	Lyα†	SB	2.72[c]	580 ± 7	3.6 ± 2.5	...	28.0 ± 3.6	17.1 ± 4.2	7.5 ± 4.8	118.6 ± 8.8	$(3.9^{+0.8}_{-0.7}) \times 10^{13}$	85.6 ± 6.1
1HERMES X1.4 J104701.68+590447.6...	4.232[L]	Lyα†	SB	−99[c]	1000 ± 8	...	...	26.2 ± 3.5	12.0 ± 4.2	4.7 ± 4.8	81.8 ± 12.2	$(4.1^{+0.9}_{-0.7}) \times 10^{13}$	99.9 ± 7.2
1HERMES X1.4 J104707.69+585149.1...	4.677[D]	Lyα†	SB	2.74[c]	...	7.1 ± 2.7	...	14.5 ± 3.6	31.5 ± 8.5	0.0 ± 10.7	36.0 ± 6.3	$(2.6^{+1.2}_{-0.8}) \times 10^{13}$	80.2 ± 17.8
1HERMES X1.4 J104709.60+590951.1...	2.942[L]	Lyα†	SB	−99[c]	...	5.9 ± 2.6	16.9 ± 4.9	13.0 ± 3.5	0.0 ± 5.2	0.0 ± 4.8	99.0 ± 11.2	$(7.8^{+7.6}_{-3.8}) \times 10^{12}$	61.0 ± 21.7
1HERMES X1.4 J104722.56+590111.7...	4.521[D]	Lyα†	SB+AGN	2.24[c]	444 ± 7	2.8 ± 2.5	...	19.0 ± 3.5	21.6 ± 4.1	17.7 ± 5.3	73.7 ± 9.4	$(2.0^{+2.1}_{-1.0}) \times 10^{13}$	45.2 ± 15.6
1HERMES X1.4 J123536.28+623019.9...	3.380[D]	Diffuse Lyα†	SB	...	...	...	...	27.1 ± 4.5	25.0 ± 4.8	17.7 ± 4.1	18.0 ± 51.7	$(1.5^{+1.3}_{-0.7}) \times 10^{13}$	47.1 ± 18.3
1HERMES X1.4 J123622.58+620340.3...	3.579[D]	Lyα; C IV†	SB	...	...	...	...	9.6 ± 4.5	26.9 ± 5.6	16.0 ± 4.3	312.5 ± 35.3	$(9.7^{+16}_{-6.1}) \times 10^{12}$	34.7 ± 17.1
1HERMES X1.4 J123732.66+621013.4...	4.019[D]	Lyα	SB	...	...	...	...	16.4 ± 4.5	9.7 ± 4.9	1.1 ± 5.3	36.5 ± 8.4	$(2.9^{+0.8}_{-0.6}) \times 10^{13}$	100 ± 2.0
1HERMES X24 J160539.72+534450.3...	3.546[D]	Lyα†	SB	−99[b]	251 ± 16	...	...	16.2 ± 4.3	16.9 ± 4.4	20.4 ± 4.6	...	$(1.3^{+0.4}_{-0.3}) \times 10^{13}$	45.4 ± 5.1
1HERMES X24 J160545.99+534544.4...	2.555[D]	Si IV; C IV; C III]	QSO	2.31[b]	670 ± 17	...	...	51.5 ± 4.7	41.8 ± 4.5	31.2 ± 5.2	...	$(1.4^{+0.2}_{-0.2}) \times 10^{13}$	39.6 ± 2.0
1HERMES X24 J160603.63+541245.1...	3.331[D]	Diffuse Lyα†	SB	−99[b]	323 ± 16	...	...	15.5 ± 4.3	16.0 ± 4.4	8.3 ± 4.9	...	$(1.0^{+0.3}_{-0.2}) \times 10^{13}$	60.6 ± 6.7
1HERMES X24 J160639.40+533558.4...	3.801[D]	Lyα	SB	−99[b]	188 ± 17	...	...	9.0 ± 4.5	16.3 ± 4.4	14.6 ± 4.8	...	$(1.1^{+0.6}_{-0.4}) \times 10^{13}$	47.1 ± 7.3
1HERMES X24 J160802.63+542638.1...	3.415[D]	Lyα	SB+AGN	−99[b]	442 ± 18	...	...	32.7 ± 4.3	35.9 ± 4.6	37.9 ± 4.5	...	$(2.2^{+0.3}_{-0.3}) \times 10^{13}$	42.5 ± 2.5
1HERMES X24 J160806.56+542301.6...	3.721[D]	Lyα; Si IV; C IV†	SB+AGN	−99[b]	246 ± 16	...	...	9.8 ± 4.3	7.4 ± 4.6	16.8 ± 4.6	...	$(1.3^{+0.7}_{-0.4}) \times 10^{13}$	49.8 ± 7.5
1HERMES X24 J161506.65+543846.9...	4.952[D]	Lyα†	SB	1.94[b]	720 ± 174	...	...	73.1 ± 4.3	49.6 ± 4.4	22.8 ± 4.8	...	$(1.2^{+0.2}_{-0.2}) \times 10^{14}$	86.2 ± 12.2

Notes. Superscripts in the z_{spec} column indicate the instrument with which the spectroscopic redshift was obtained, LRIS (L) or DEIMOS (D). *Herschel*-PACS photometry comes from PEP (Lutz et al. 2011) in COSMOS and from HerMES (Oliver et al. 2012) in Lockman Hole North. Photometric redshifts come from: [a]Ilbert et al. (2010) in COSMOS; [b]Rowan-Robinson et al. (2008) in ELAIS-N1; [c]Strazzullo et al. (2010) in Lockman Hole North; and [d]Cardamone et al. (2010) in ECDF-S. The galaxy "Class" column describes the rest-frame ultraviolet spectrum as Lyman Break Galaxy (LBG), quasar (QSO), starburst (SB), or starburst with AGN (SB+AGN). Ellipsis in S_{24}, S_{100}, S_{160}, $S_{1.4}$, or z_{phot} columns denotes that the source is undetected at the corresponding wavelength or has no photometric redshift despite having the necessary optical imaging, whereas − denotes that no data exist. Sources marked with a † in the comments are classified as spectroscopically tentative, and excluded from the "high confidence" SFRD estimate (see Section 5).

identified at $2 < z < 5$. In each case, the S/N of the identifying feature (Lyα emission in the majority of cases) is required to be >5 in the two-dimensional spectrum. The two-dimensional spectra for Lyα-identified sources are shown in Figure 2. Note that the S/N of Lyα changes from the two-dimensional spectra to one-dimensional extractions of the spectra depending on the sources' compactness, the compactness of continuum relative to Lyα emission, and the observed wavelength of the line. For example, one-dimensional extractions with Lyα longward of ~6000 Å are prone to contamination by the OH forest, thus will be of significantly poorer quality in one dimension than in two dimensions where OH features are more easily distinguished from real lines.

Initially, we split sources into two categories: sources with multiple spectroscopic features (e.g., Lyα emission, Si IV absorption, C IV emission) and single-line identifications (where Lyα is identified as the only emission line). The former group of identifications is naturally more secure than the latter. The latter source list is dominated by sources at the high-redshift end, $3 \lesssim z \lesssim 5$, since multiple features are naturally more difficult to identify in higher redshift sources. However, there are clear cases where the identification of Lyα at $>5\sigma$ is more secure than the identification of multiple other features at low signal to noise ($S/N \lesssim 5\sigma$). An example of a secure single-line source is 1 HERMES X24 J160802.63+542638.1 at $z = 3.415$ where Lyα is detected at $>5\sigma$. An example of a less secure multi-feature source is 1 HERMES X1.4 J123622.58+620340.3 at $z = 3.579$ where both Lyα and C IV are detected at S/N<5σ. In this paper, we choose to segregate sources with secure spectroscopic identifications from those with tentative identifications rather than sources with single- or multi-line identifications.

Sources are categorized as "tentative" rather than "secure" if (1) the signal to noise of the Lyα feature is $5 < S/N < 7$ as measured in the two-dimensional LRIS/DEIMOS spectrum using an appropriately sized, adjustable aperture, and if (2) out of five co-authors who did a thorough quality ranking of each source's spectrum, at least three ranked the source as "tentative" rather than "secure." Figure 3 show all rest-frame ultraviolet spectra for all 36 sources in the sample.

Tentative sources are marked with a dagger (†) in Table 1 and denoted as "tentative" in Figures 2 and 3. Out of 36 sources, we classify 22 as secure and 14 as tentative. Note that one source 1HERMES X1.4 J100024.00+021210.9 at $z = 3.553$ is classified as tentative *not* because the Lyα emission is of low S/N, but because there is peculiarly strong emission from Si IV relative to Lyα and C IV; this could be an artifact of the noise, but since it is particularly unusual, we have categorized this source as tentative.

Photometric redshifts are used, when available, to verify spectroscopic redshifts to within $\Delta z/(1+z) \sim 1/2$ (Ilbert et al. 2010; Rowan-Robinson et al. 2008; Strazzullo et al. 2010; Cardamone et al. 2010). This threshold is not strict, but rather used to spot egregious disagreements between spectroscopy and photometry. These photometric redshift catalogs are of varying quality depending on the depth and number of optical and near-infrared bands available, from the limited and shallow coverage in EN1 to the extensive 30-band coverage in COSMOS. The loose constraint of agreement between photometric and spectroscopic redshift is based on the fact that photometric redshifts are notoriously unreliable for dusty starbursts. Even in the deepest multi-band fields like COSMOS, ~30% of Spire sources do not have photometric redshifts (e.g., Mobasher et al. 2007; Ilbert et al. 2010).

Viewing geometry can have a very strong impact on the relative fractions and wavelengths of escaped ultraviolet/optical light (Siana et al. 2007, 2010; Scarlata et al. 2009). Heavy obscuration can have dramatic impact on photometric redshift reliability in two ways. First, by obscuring rest-frame ultraviolet and optical light so much that the source has an artificially high photometric redshift (i.e., the source is thought to drop out due to redshifting rather than reddening). Second, dusty sources often have differential absorption of Lyα photons and non-resonantly scattered continuum photons (e.g., the "UV chimney" argument; see Neufeld 1991), resulting in artificially low photometric redshifts.

Even in the lower redshift samples (C12), sources with very confident photometric redshifts from the multi-band data of COSMOS and CDFS have photometric redshift accuracy of $\Delta z/(1+z) = 0.29$. This highlights the lack of reliability in photometric redshifts of dusty galaxies. Therefore, the primary purpose of the photometric redshift restriction in this paper is to verify that the detected emission line is in fact Lyα and not [O II] (which would correspond to redshifts between 0 and 1). Fifteen of the 36 sources do not have photometric redshifts—even though some of them lie in areas of very deep ancillary data—a testament to their dusty and optically obscured nature. The sources with fewer identifiable spectral signatures in our spectra are less optically luminous than those with multiple features. Those that are optically fainter will have less reliable photometric redshifts and are more likely to be categorized here as tentative.

3.1. Alternate Redshift Identifications

Figure 4 plots photometric redshift against spectroscopic redshift where photometric redshifts are available. The distribution in spectroscopic redshift of sources without photometric redshift is the gray histogram. Alternate redshifts, assuming the emission lines are actually [O II] instead of Lyα, are shown as crosses in Figure 4. The [O II]-implied spectroscopic redshifts are less consistent with photometric redshifts than the Lyα-implied spectroscopic redshifts. This makes sense in the context of the probable enhanced Lyα-to-continuum ratios in these galaxies.

While our identified Lyα emission lines could also be Mg II (2798 Å), Mg II would be suggestive of a strong active galactic nucleus (AGN). With AGN, other features (e.g., C III] 1909 Å and [O II]) would also be detectable. Given the expected relative strengths of Mg II relative to [O II], C III], C IV, and Lyα, Mg II is unlikely to be identified as the only discernible feature. In the case of [O II], both [O III] and Hβ emission lines and/or Ca H & K absorption, or the 4000 Å break features are expected. Also at wavelengths >6000 Å, the [O II] doublet is resolvable with LRIS and DEIMOS. In comparison to our lower redshift sample (C12), for which there are ~500 [O II] identified lines at the same wavelengths, the sources in this paper have none of the above signatures which would point to a misidentification as [O II].

Also note that if the Lyα-identified lines were actually [O III] or Hβ they would sit at even lower redshifts than they would if they were [O II]. Because there are no sufficiently bright emission lines between Lyα (1216 Å) and [O II] (3727 Å) for starbursts, it is straightforward to segregate between $z > 2$ and $0 < z < 1$ sources using photometric redshift.

We inspect the optical images of each source that does not have a photometric redshift to judge the plausibility

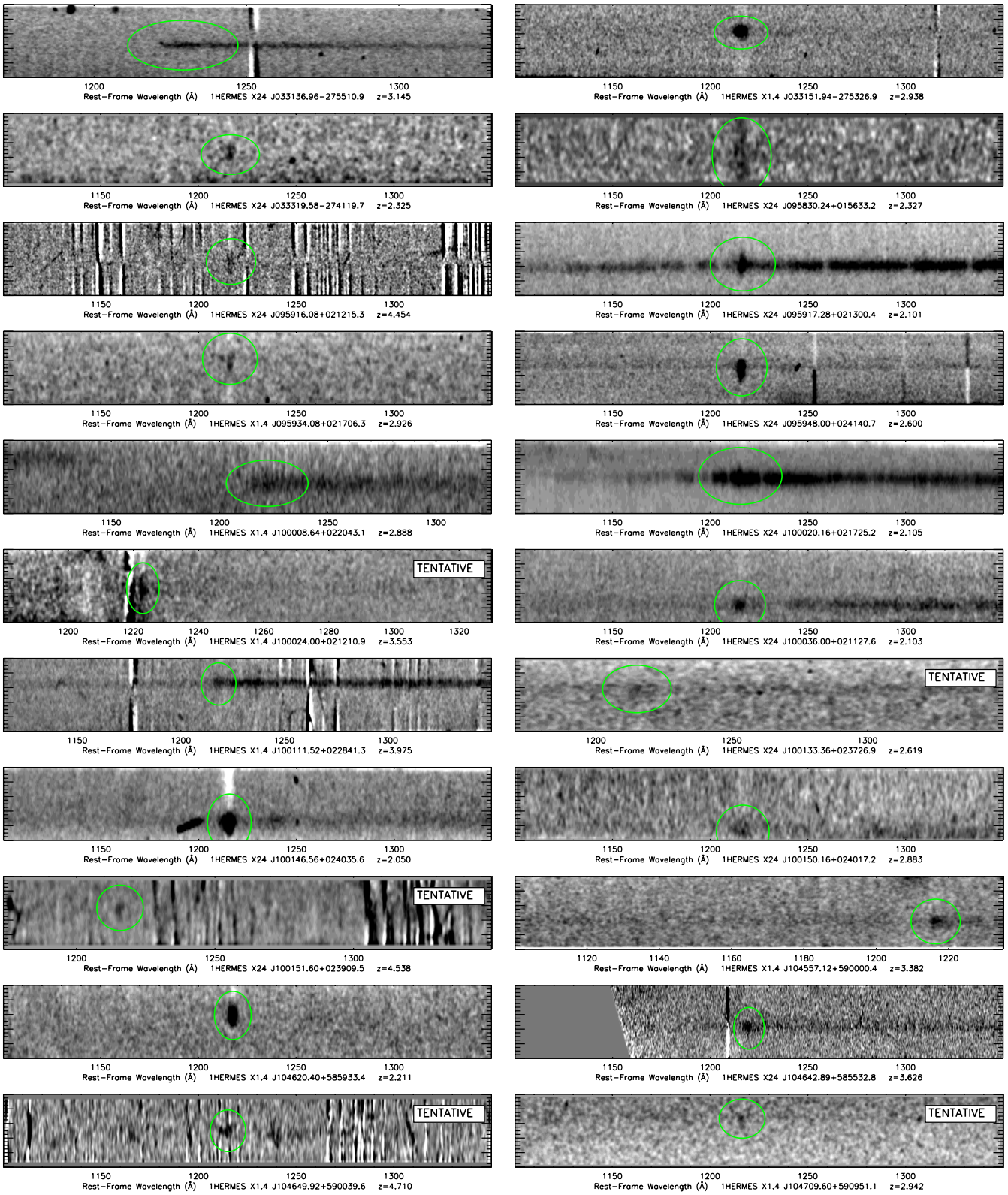

Figure 2. Two-dimensional spectra around the identified Lyα features for the sources only identified through a single emission line. This emission line is not thought to be [O II] or Mg II in these cases since there is no detection of commonly bright, accompanying emission lines, e.g., [O II], [O III], and Hβ, within the wavelength coverage of LRIS/DEIMOS observations. Note the wide variety of Lyα morphologies, from very diffuse to very compact, with and without redward continuum. The sources at higher redshifts are observed at higher wavelengths, thus likely have one-dimensional extractions contaminated by the OH forest.

(A color version of this figure is available in the online journal.)

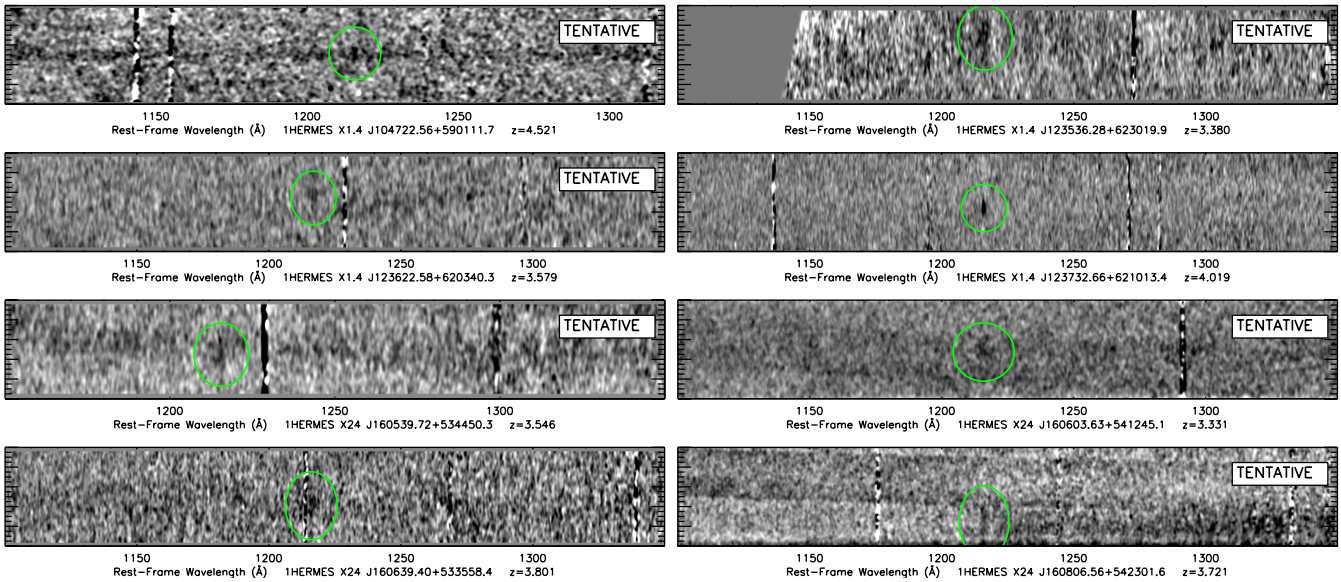

Figure 2. (Continued)

of our identifications. All three GOODS-N sources are *u*-band dropouts. Both 1HERMES X1.4 J123622.58 and 1HERMES X1.4 J123732.66 are also *b*-band dropouts (the two higher redshift sources), and all three have optical photometry that is consistent with their spectroscopic identifications. Of the eight LHN sources without photometric redshifts, 1HERMES X1.4 J104557.12 is compact and has $i \approx 24.5$, 1HERMES X1.4 J104701.68 and 1HERMES X1.4 J104709.6 have $i \approx 24.3$, 1HERMES X1.4 J104722.6 and 1HERMES X1.4 J104707.7 have $i \approx 25$, and 1HERMES X1.4 J104620.4, 1HERMES X24 J104642.9, and 1HERMES X1.4 J104649.9 are *i*-band dropouts. These magnitudes do not rule out the possibility that these are low-redshift sources, but indicate consistency between our high-z spectroscopic identifications and photometry. In COSMOS, only one source, 1HERMES X24 J100133.36+023726.9, has no photometric redshift since it drops out in all images. Elais-N1 sources have much shallower photometric coverage than the other fields, hence there are more sources without photometric redshifts. While all sources are detectable in wide *i*-band imaging, multi-band imaging is not available across the whole field. None of the sources are sufficiently bright or extended in the *i* band to be a convincing $z < 1$ identification.

Note that 1HERMES X24 J161506.65+543846.9, the highest redshift source in our sample at $z = 4.95$, has an odd assortment of photometric measurements, dropping out in all wavebands (including the z band) except the *i* band, where it has a magnitude of 22.8 (AB). The low photometric redshift ($z_p = 1.94$) is likely caused by this peculiar optical spectral energy distribution (SED), but is also perfectly consistent with Lyα in the *i* band at $z \sim 5$, and enhanced Lyα-to-continuum ratios (Neufeld 1991). We also note that this source is classified as tentative.

4. SAMPLE CHARACTERISTICS

The importance and context of the $2 < z < 5$ HSG population can only be judged with a basic understanding on the physical characteristics of the sample. Here we measure those physical characteristics, compare them to the properties of other galaxy populations, and assess the impact of infrared selection biases on our interpretation.

4.1. SED Fits, Luminosities, and Dust Temperatures

The infrared photometry summarized in Table 1 is fit with an FIR SED consisting of a coupled single dust temperature-modified blackbody and mid-infrared power law such that

$$S(\lambda) = N_{\rm bb} \frac{\left(1 - e^{-\left(\frac{\lambda_0}{\lambda}\right)^{\beta}}\right)\left(\frac{c}{\lambda}\right)^3}{e^{hc/\lambda kT} - 1} + N_{\rm pl}\,\lambda^{\alpha}\,e^{-\left(\frac{\lambda}{\lambda_c}\right)^2}, \quad (1)$$

where $S(\lambda)$ is in units of Jy and T is the galaxy's characteristic "cold" dust temperature (the dust temperature dominating most of the infrared luminosity and dust mass). The emissivity index is represented by β, and λ_0 is the wavelength at which optical depth is unity (here fixed at $\lambda_0 = 200$ μm, as described in Conley et al. 2011). The slope of the mid-infrared power-law component is given by α, and λ_c is the wavelength where the gradient of the modified blackbody is equal to α. $N_{\rm bb}$ and $N_{\rm pl}$ are the coefficients of the modified blackbody and power laws, respectively. $N_{\rm pl}$ is a fixed function of $N_{\rm bb}$, α, and T such that the power law and modified blackbody are continuous at λ_c. This SED fitting method is described fully in Casey (2012), and is also discussed in C12 as applied to the low-redshift population. It is given in related forms in Blain et al. (2002, 2003), Younger et al. (2009), and Conley et al. (2011).

To reduce the number of free parameters, we fix $\alpha = 2.0$ for sources without PACS photometry and $\beta = 1.5$ for all (the measured values found for local *IRAS* and some distant ULIRGs; Casey 2012). These leave two free parameters: $N_{\rm bb}$, which effectively scales with $L_{\rm IR}$, and T, the temperature of the modified blackbody. We remeasure dust temperatures for each galaxy by determining the wavelength where the flux density peaks and convert that to a dust temperature via Wien's Law. This provides a more consistent measure of dust temperature, which can be used in comparisons between SEDs fit with alternate techniques, using model templates or direct fits (Chary & Elbaz 2001; Dale & Helou 2002; Blain et al. 2003; Siebenmorgen & Krügel 2007; Draine & Li 2007; Kovács et al. 2010). We compute infrared luminosities by integrating

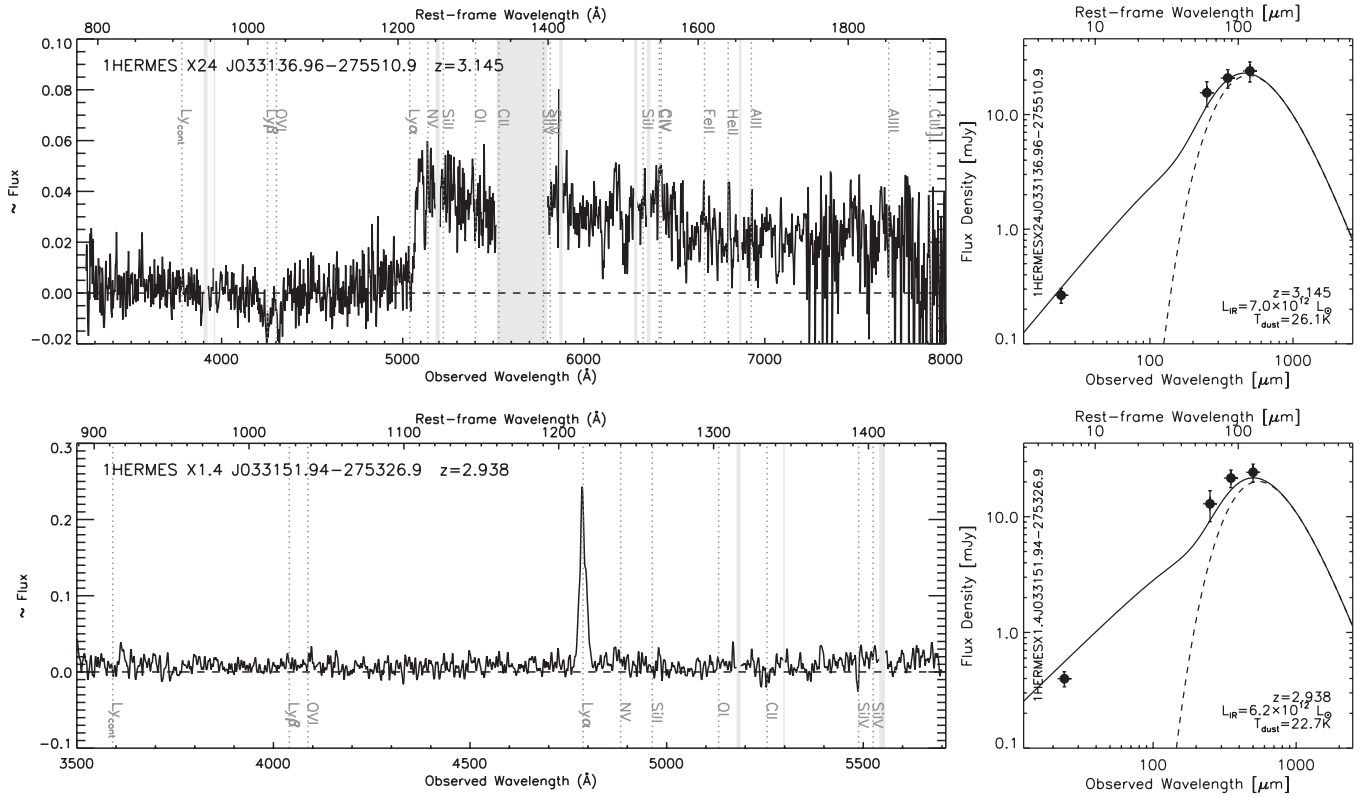

Figure 3. One-dimensional spectra of $z > 2$ Spire sources in observed wavelength shown in the left panels. The flux scaling is arbitrary. The wavelengths of rest-frame ultraviolet features are marked by vertical dotted gray lines with noted names. All lines are shown irrespective of whether or not they are seen in emission or absorption, and whether or not they are detected. Redshifts are measured off of the Lyα redshift in all cases where Lyα is detected (a minority of sources is identified by C IV emission). The Lyα redshifts are typically redshifted with respect to other spectral features, which is evidence of stellar winds (to be discussed at more length in a future paper). Right panels show best-fit far-infrared spectral energy distributions to infrared photometry. The total SED is a solid line while the underlying cold-dust-modified blackbody is a dashed one. The derived IR luminosities and dust temperatures are shown.

the above best-fit SED between 8 and 1000 μm. The SED fits are shown alongside the sources' optical spectra in Figure 3, and their infrared luminosities and dust temperatures are given in Table 1.

The luminosities of this sample range from 3.2×10^{12}–6.3×10^{13} $L_\odot$, implying infrared SFRs of 500–9000 $M_\odot$ yr^{-1} (with one outlier at 1.6×10^{14} $L_\odot$, 26000 $M_\odot$ yr^{-1}, whose redshift is tentative). Most galaxies in the sample have SFRs an order of magnitude beyond the extreme activity seen in ULIRGs (which have SFR $\approx$ 200–1000 $M_\odot$ yr^{-1} by the scaling given in Kennicutt 1998). These starbursts are among the most extreme star-forming galaxies seen in the universe (among other HyLIRG populations; Rowan-Robinson 2000; Bridge et al. 2012).

The conspicuously high SFRs (e.g., above $\sim$1000 $M_\odot$ yr^{-1}) might lead us to believe that AGNs contaminate the FIR luminosity or rather that there is potential variation in star formation laws at high redshift. There has been some recent discussion of whether or not the Kennicutt (1998) scaling between IR luminosity and SFR holds under "extreme" conditions or at high redshifts (Swinbank et al. 2008). Assuming a modified initial mass function (IMF) would produce more modest SFRs than the default Salpeter IMF. This might change our interpretation and change the SFRs we measure here, so we use the Kennicutt scaling for SFRs in this paper to be consistent with literature work.

Figure 5 shows the infrared luminosity against dust temperature for the HSG sample. There is a noticeable absence of very warm sources at lower luminosities. Similarly, there are very few cold sources at high luminosities. This is primarily a consequence of selection effects in the SPIRE bands. Warm-dust galaxies are selected against in the SPIRE bands, even at these high-redshifts, due to the sensitive variation of infrared flux density measurements with dust temperature; the dashed lines illustrate the lower luminosity detection limits as a function of dust temperature, for a galaxy at $z = 2$, $z = 3$, or $z = 4$. This dust-temperature selection bias is even more exaggerated at 850 μm. The luminosity detection limits for 850 μm selection are shown as solid lines in Figure 5, nearly bisecting the SPIRE population so that about half would be 850 μm undetected). Before *Herschel*, the cold-dust temperature bias of submillimeter observations was the focus of many studies looking for the elusive "warm-dust" SMGs (Blain et al. 2004; Chapman et al. 2004a, 2010; Casey et al. 2009, 2011a; Magdis et al. 2010; Chapin et al. 2011).

Figure 6 plots HSGs' infrared luminosities against redshift relative to the detection limits of the selection wavelengths: the three 250, 350, and 500 μm SPIRE bands, 24 μm and 1.4 GHz. The detection limits in the SPIRE bands depend on the assumed SED shape and dust temperature, which is not uniform for all SPIRE-selected galaxies. We use the distribution of measured dust temperatures in Figure 5 to set limits on the detection boundaries in $L_{\rm IR}$–z in Figure 6. In other words, we measure the mean dust temperature for 250 μm selected galaxies to be 40 K, for 350 μm selected galaxies as 39 K, and for 500 μm selected galaxies as 37 K. Differences on the scale of a few degrees are negligible for these illustrative boundary lines in Figure 6, so we adopt a 40 K SED for all three selection boundaries.

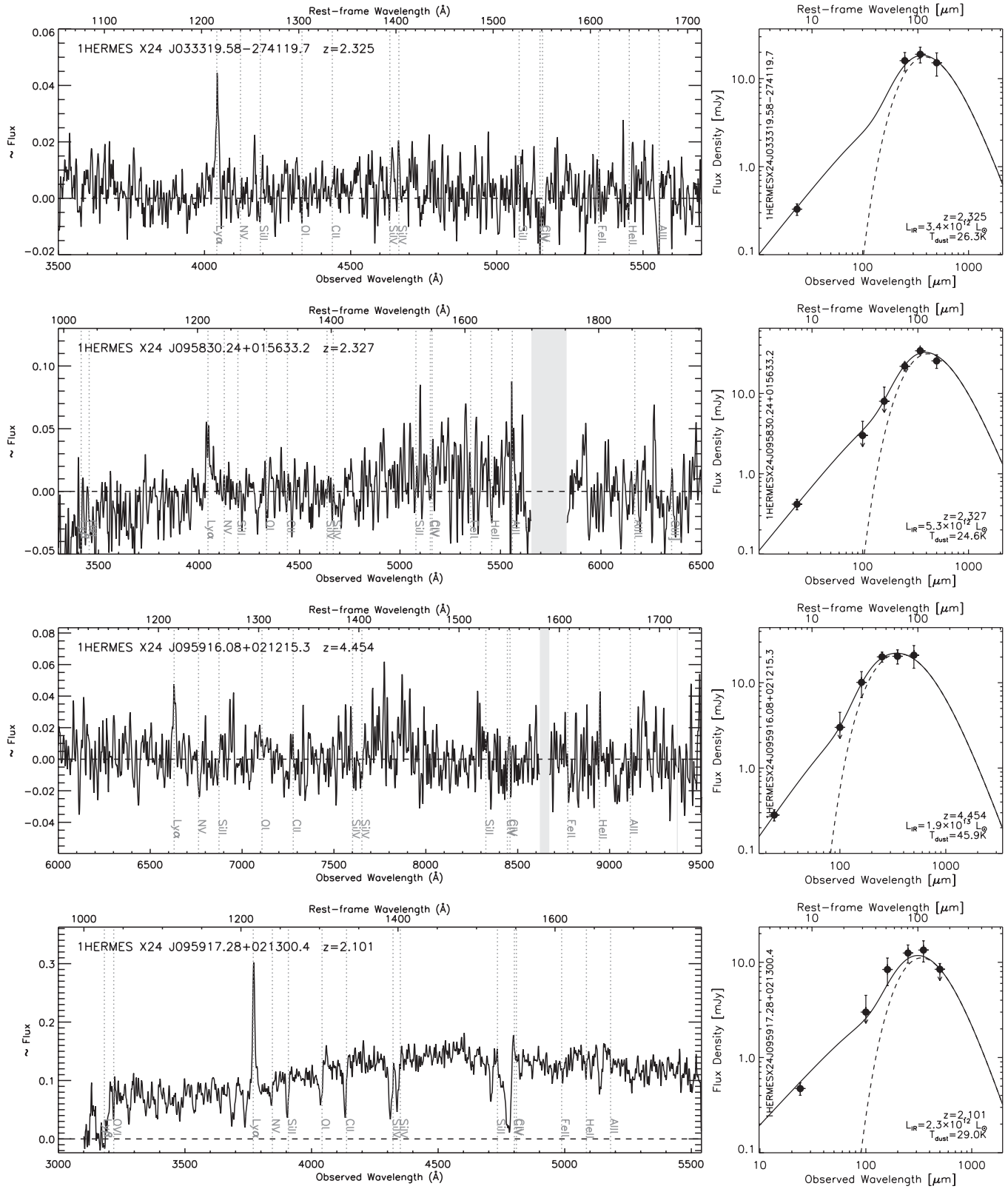

Figure 3. (Continued)

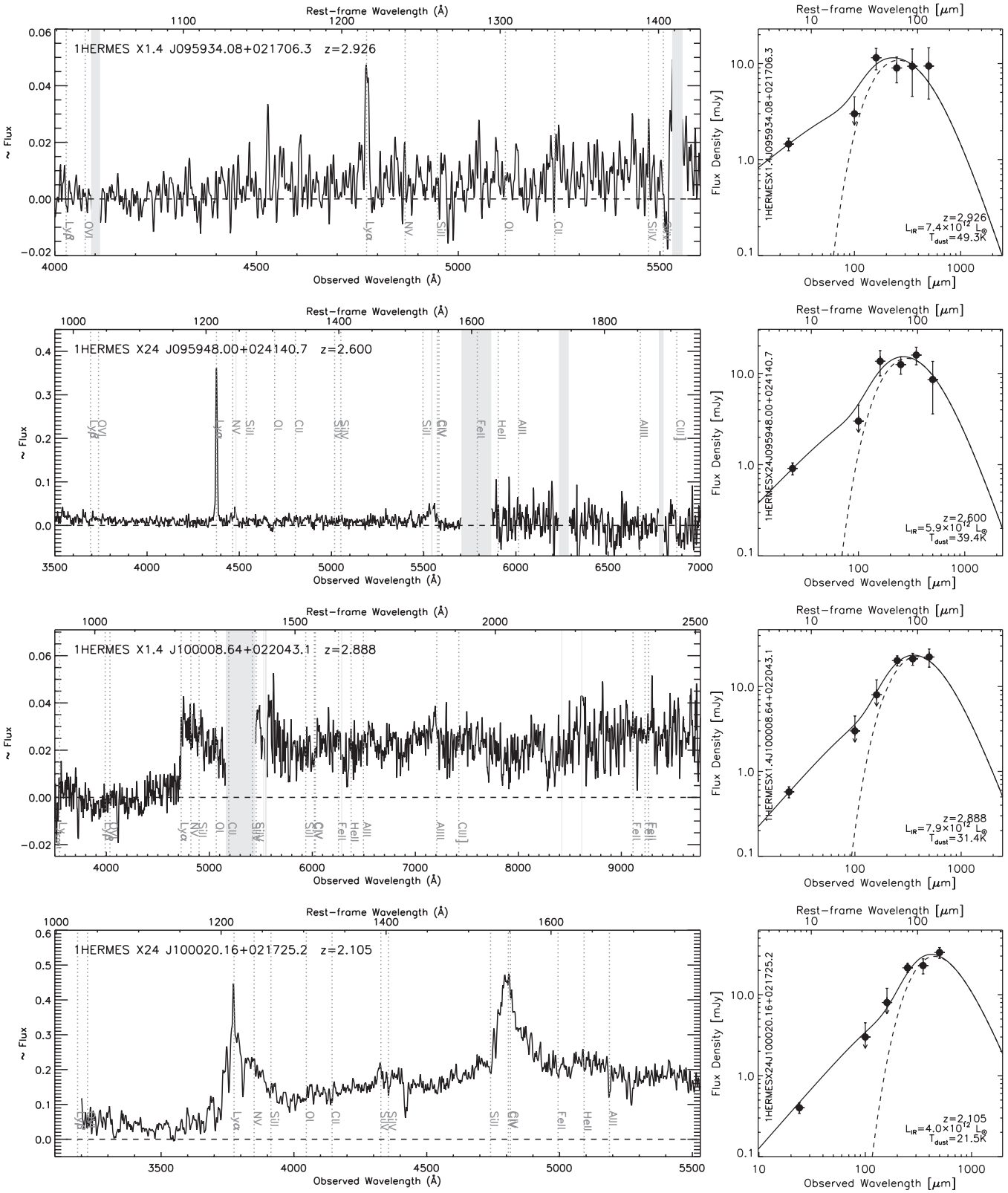

Figure 3. (Continued)

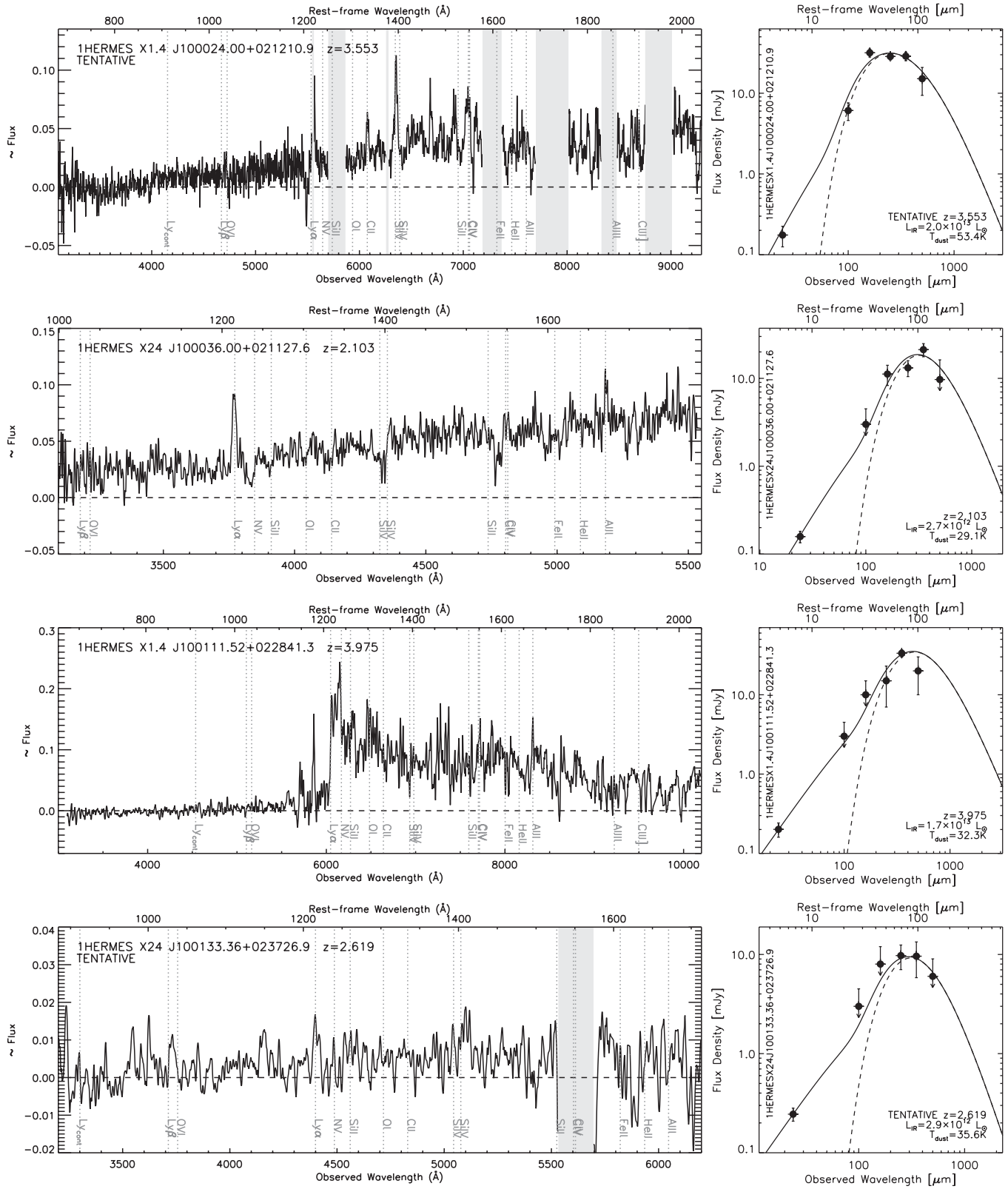

Figure 3. (Continued)

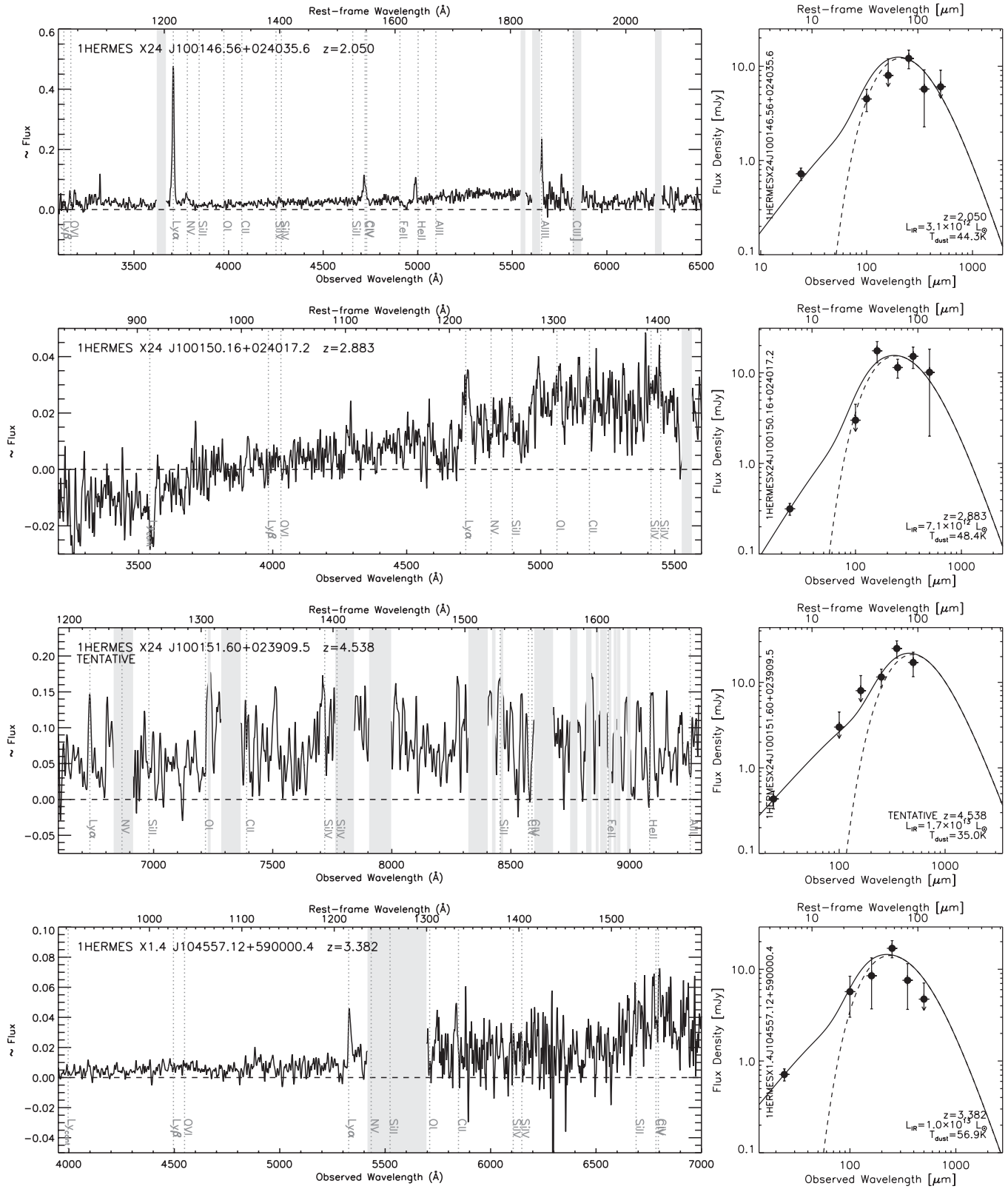

Figure 3. (Continued)

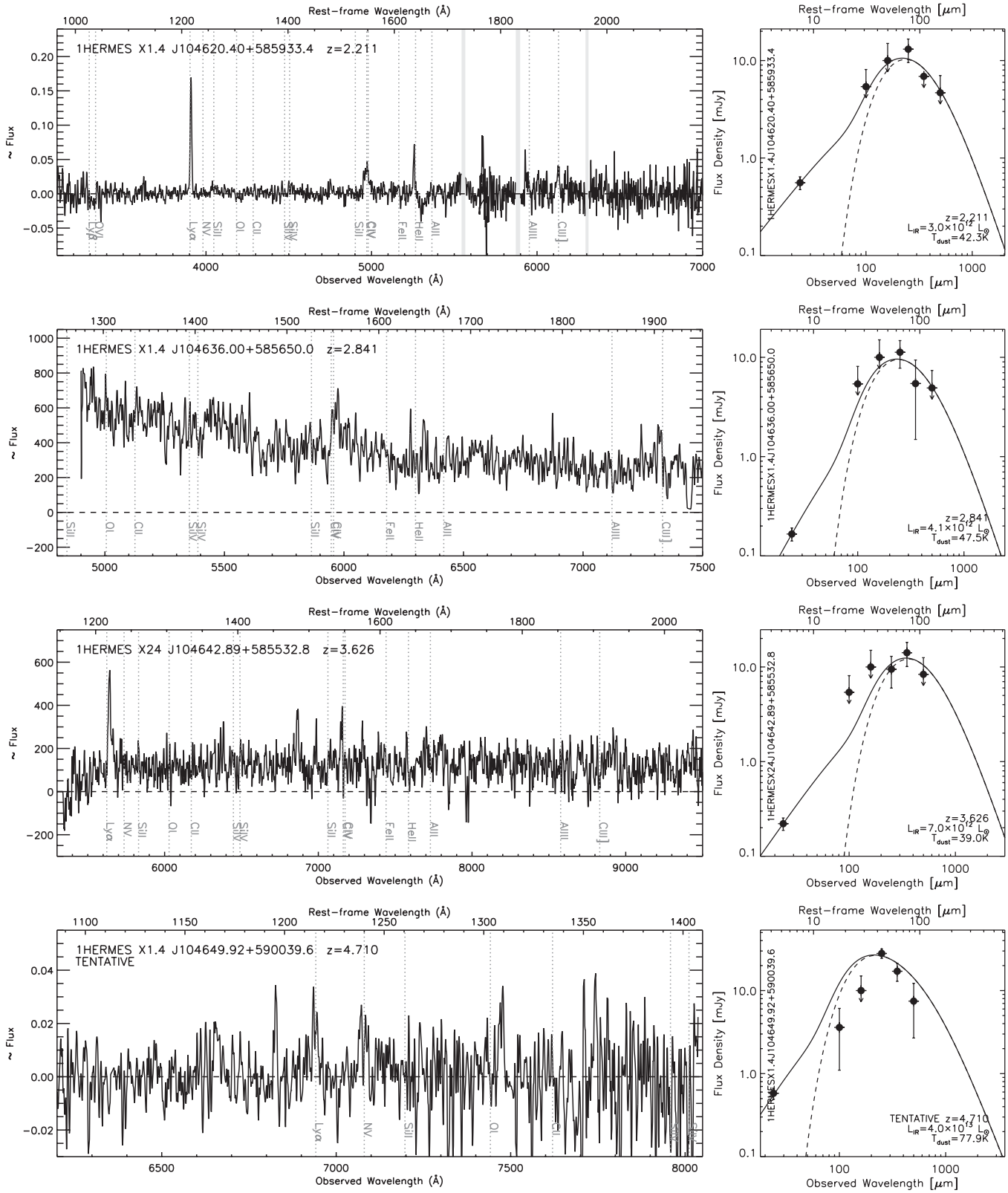

Figure 3. (Continued)

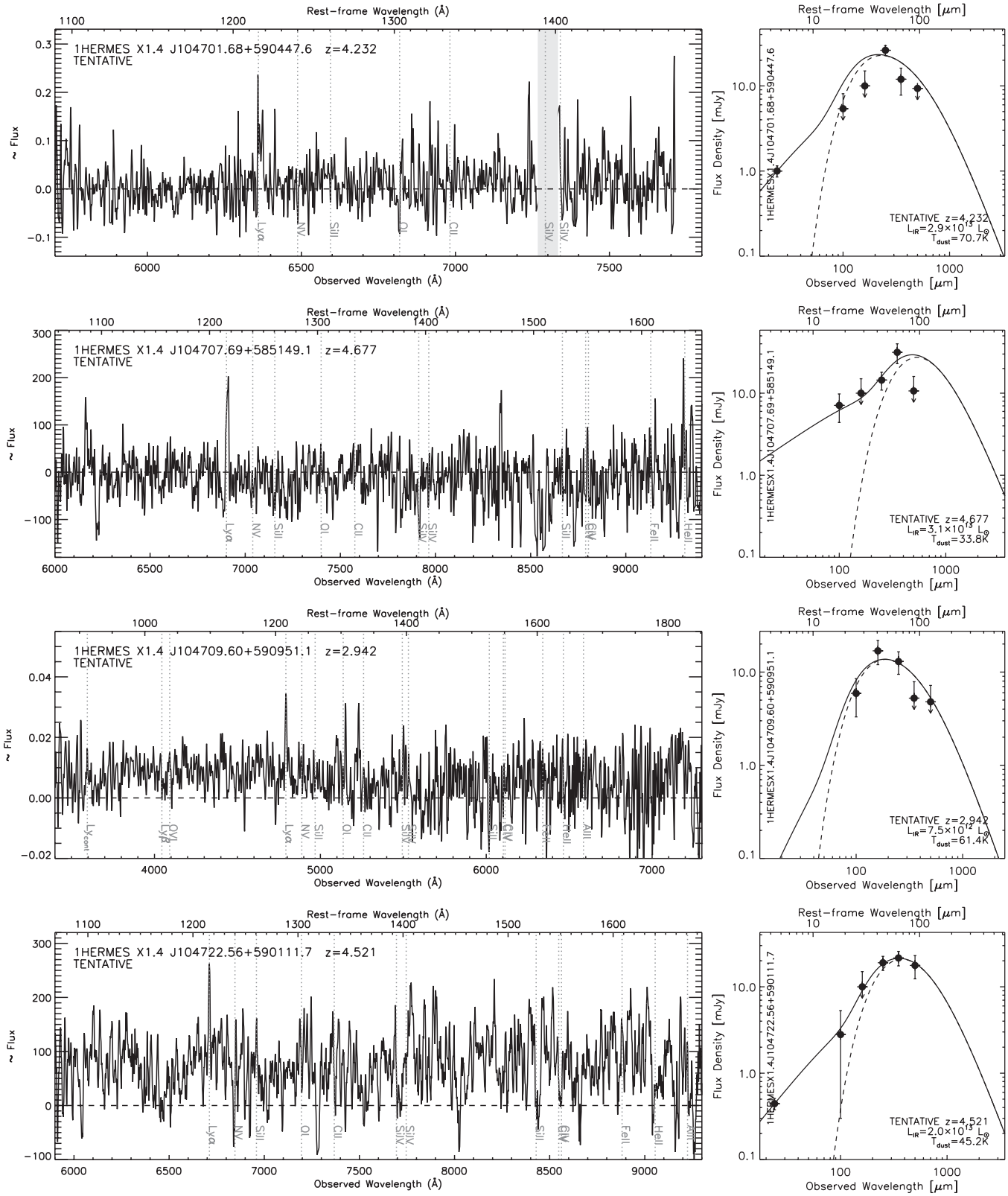

Figure 3. (Continued)

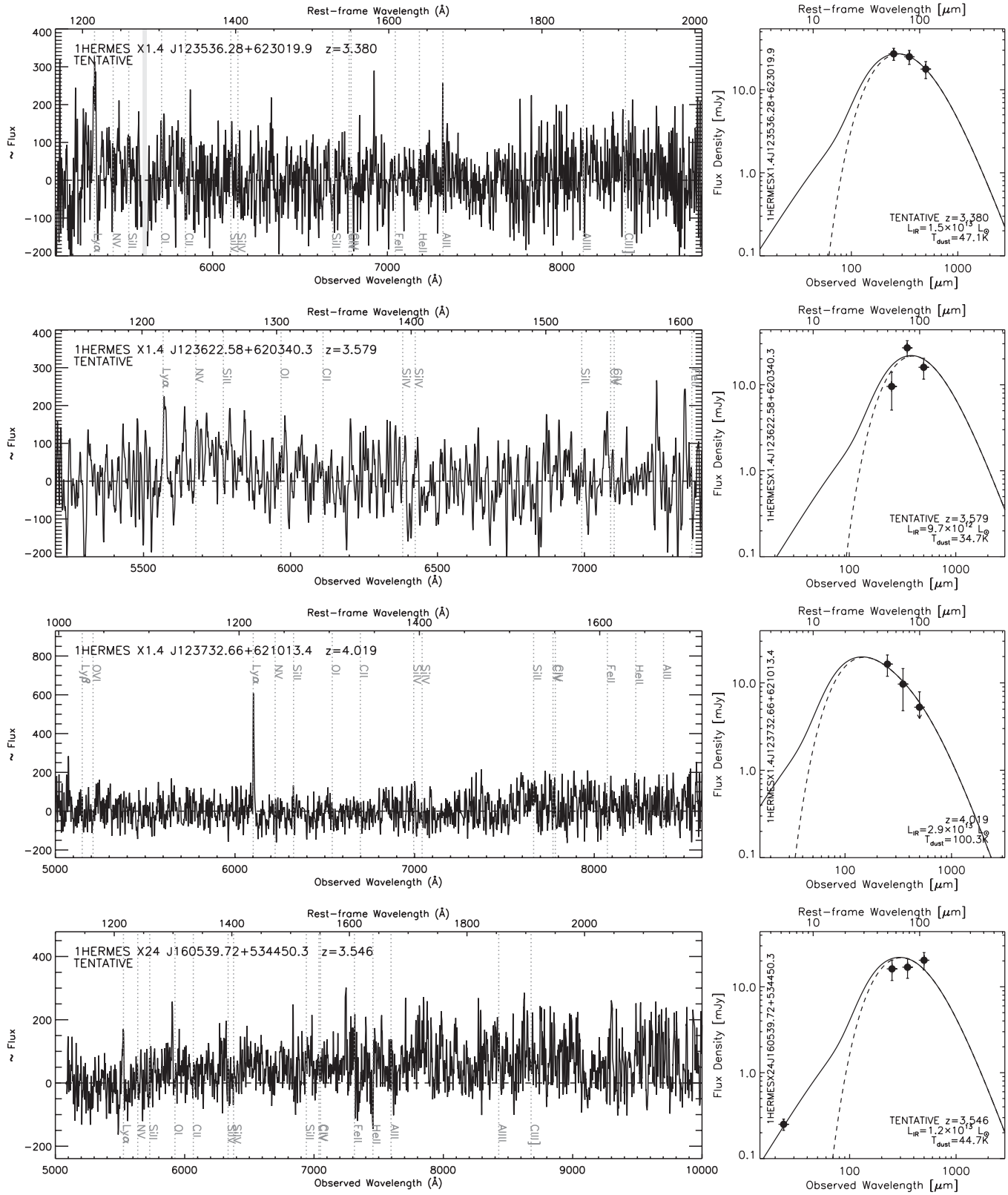

Figure 3. (Continued)

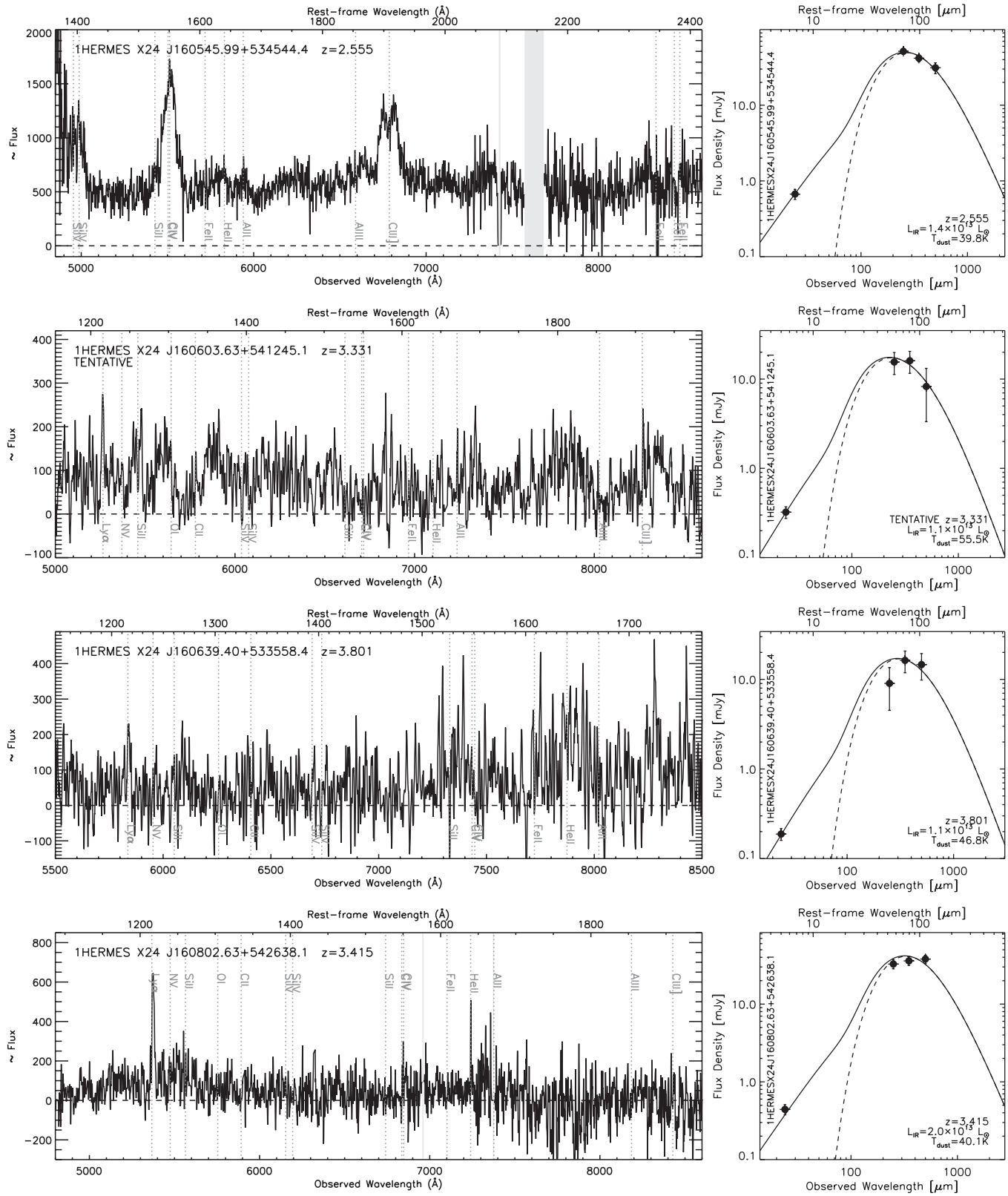

Figure 3. (Continued)

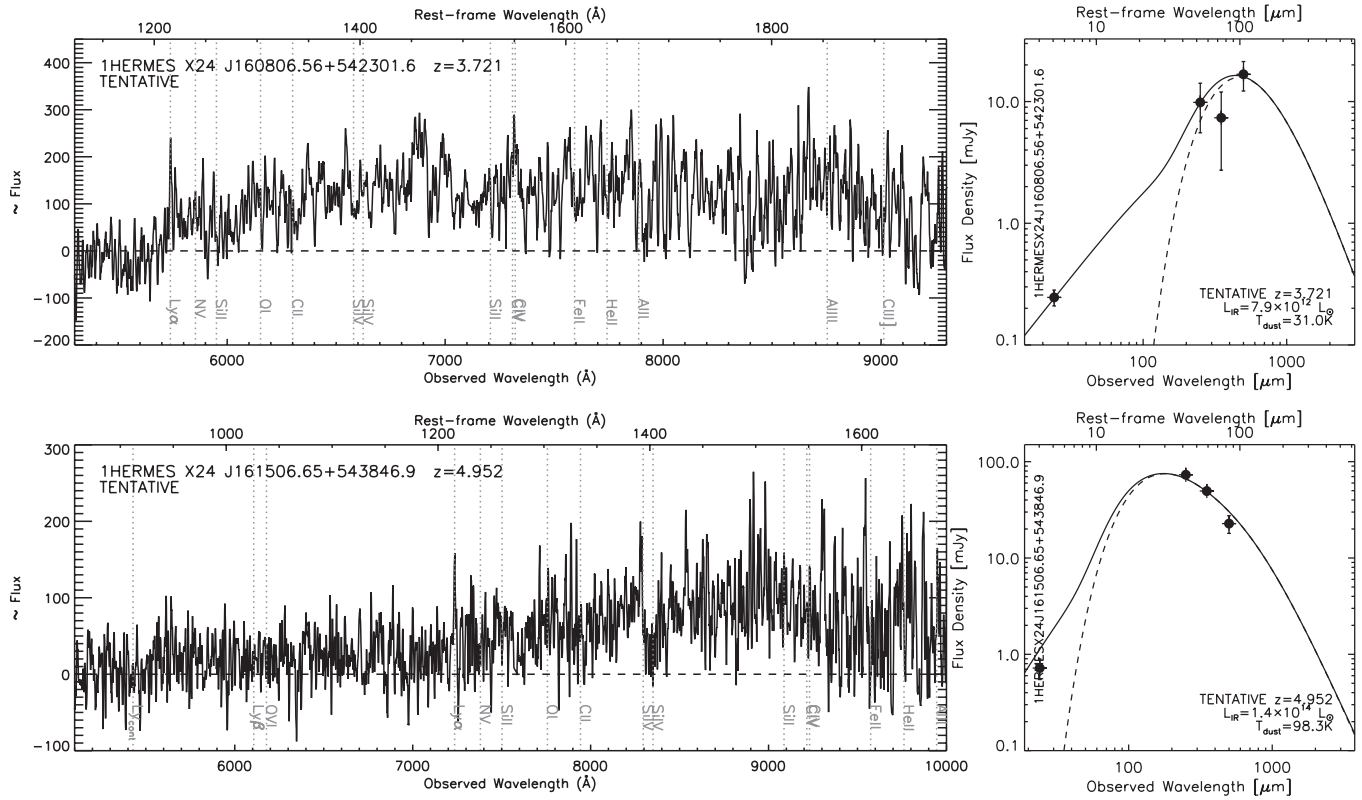

Figure 3. (Continued)

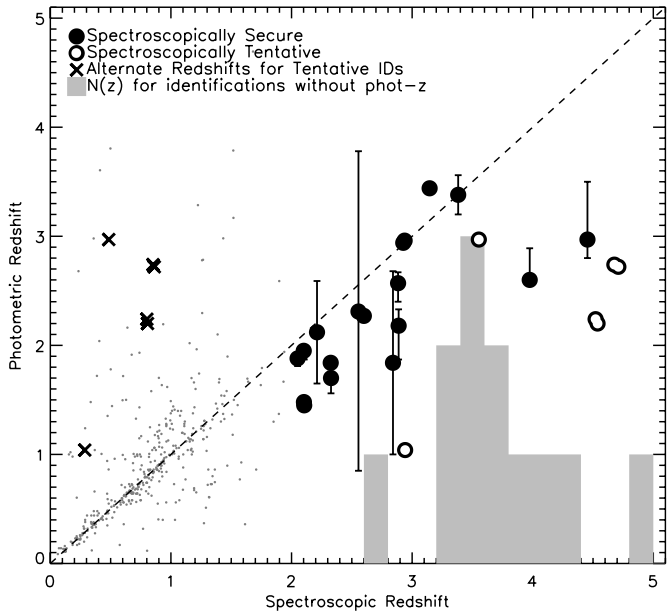

Figure 4. Spectroscopic redshift against photometric redshift for our SPIRE-selected galaxy sample. Sources with identifications based on multiple spectroscopic features (emission lines, absorption lines, breaks) are shown as black circles, while identifications made from a single feature (i.e., Lyα emission) are open circles. The photometric and spectroscopic redshifts for the full sample of 767 HSGs (C12) are shown as small gray points. Since the single-line source emission lines could have been misidentified, we also mark the corresponding spectroscopic redshifts if [O II] is assumed and find generally poor agreement with the photometric redshift (black crosses). The distribution in spectroscopic redshifts for sources with *no* photometric redshifts is shown in gray; there is no obvious trend with redshift.

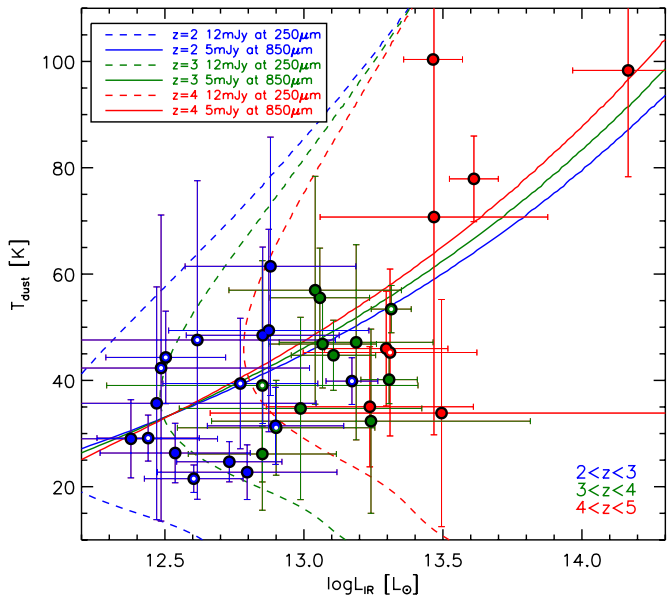

Figure 5. Infrared luminosity against dust temperature for the sample, color coded by redshift interval: $2 < z < 3$ (blue), $3 < z < 4$ (green), and $4 < z < 5$ (red). Overplotted are typical lower luminosity limit boundaries—a function of dust temperature—at a given wavelength, redshift, and flux density limit. A 12 mJy flux density limit is assumed for the SPIRE bands (dashed lines) and a 5 mJy limit is assumed at 850 μm (solid lines). This illustrates how half of the SPIRE-selected sample have dust temperatures too warm to be 850 μm detectable. Sources with AGN optical signatures are marked with small white dots at their centers.

(A color version of this figure is available in the online journal.)

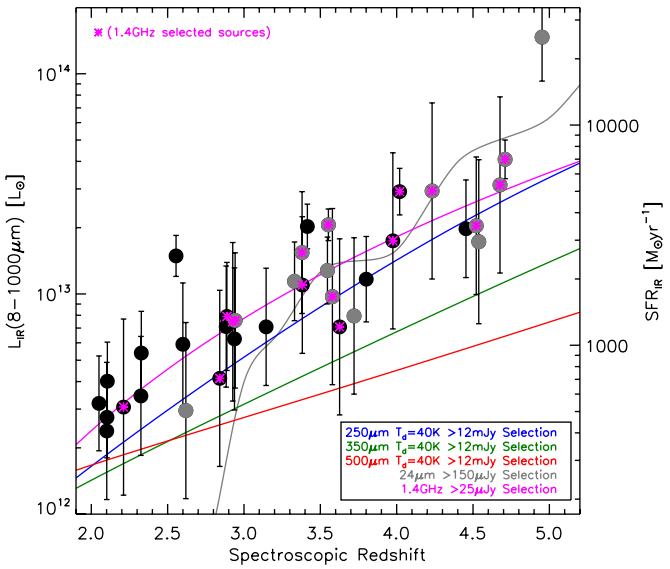

Figure 6. Integrated infrared luminosity (8–1000 μm) against spectroscopic redshift for our sample (black sources are secure and gray sources are tentative, as in Table 1). Luminosities span 2.4×10^{12}–4.0×10^{13} $L_\odot$, with one outlier at 1.4×10^{14} $L_\odot$. The detection boundaries of each selection wavelength are also illustrated as a function of redshift. The SPIRE detection boundaries assume flux densities >12 mJy and an SED dust temperature of 40 K. The radio boundary assumes that the FIR/radio correlation (Helou et al. 1985) holds with a >40 μJy radio detection limit. The 24 μm limit assumes a 150 μJy detection limit along with a typical 24 μm–L_{IR} scaling (e.g., Le Floc'h et al. 2005). Radio sources are marked by a magenta asterisk, while 24 μm sources are black.

(A color version of this figure is available in the online journal.)

Most of the fields that have radio data have a detection limit $\gtrsim$40 μJy, so we construct the radio detection boundary based on the FIR/radio correlation for starbursting galaxies (Helou et al. 1985; Condon 1992) with q_{IR} evolving as in Ivison et al. (2010b). The 24 μm detection boundary is the least certain as it scales with L_{IR}; many recent works note up to $\sim$1 dex disagreement between extrapolated 24 μm infrared luminosities and direct measurements (e.g., Le Floc'h et al. 2005, 2009; Elbaz et al. 2011). This tells us that, although we can use the 24 μm detection boundary shown in Figure 6 as a rough guide, it should not be concerning that 24 μm selected sources fall below the line by $\lesssim$0.3 dex.

Although very few of these sources have existing 850 μm data, this work (especially Figure 5) suggests that half of the SPIRE-selected population would be undetectable in the original SCUBA 850 μm surveys *even* at these redshifts. Specifically, we estimate that only 31/36 sources would have $S_{850} > 2$ mJy (86%), while only 21/36 sources have $S_{850} > 5$ mJy (58%). The statistics of the temperature-bias selection effect are discussed in more detail in C12, as they relate to the lower redshift population where the statistics are more robust.

4.2. FIR/Radio Correlation

For the 23 radio-detected sources, we investigate the FIR/radio correlation for starburst galaxies (Helou et al. 1985; Condon 1992). Measuring the FIR/radio correlation in this sample is useful for checking that our sample is roughly consistent in FIR/radio given expectation from our measured redshifts (i.e., it is another reassurance on tentative identifications in particular). This correlation is measured via the ratio of FIR luminosity to radio luminosity such that

$$q_{IR} = \log\left(\frac{1.02 \times 10^{18}\, L_{FIR}}{4\pi\, D_L^2}\left[\frac{cm^2}{L_\odot}\right]\right) - \log(1 \times 10^{-32}\, S_{1.4}\,(1+z)^{\alpha-1}[\mu Jy^{-1}]), \quad (2)$$

where L_{FIR} is the far-infrared luminosity measured in the range 40–120 μm given in $L_\odot$, D_L is the luminosity distance in cm, $S_{1.4}$ is the 1.4 GHz flux density in μJy, and α is the synchrotron slope, here set to 0.75 (Ibar et al. 2010; Ivison et al. 2010a) and defined such that $S_\nu \propto \nu^{-\alpha}$.

Twenty-three of the 36 galaxies in our sample are radio detected (64%), and their measured q_{IR} ranges from 0.7 to 2.1 with mean value $\langle q_{IR} \rangle = 1.58 \pm 0.35$. Note that the infrared luminosity component in q_{IR} is L_{FIR}(40–120), not L_{IR}(8–1000). If L_{IR}(8–1000) is used instead, luminosities and q increase by 0.40 ± 0.15 dex and the scatter in q grows; the increased scatter is caused by the contribution from the mid-infrared flux to L_{IR}. Only one galaxy in our sample is "radio-loud" and indicative of an AGN (the source at $z = 3.579$); this is consistent with the observed C IV emission in its rest-UV spectrum. We observe that the rest of the radio-detected sample agrees within uncertainties with previous measures of $q_{IR}(z)$ in previous samples (Ivison et al. 2010a; Kovács et al. 2010; Magnelli et al. 2012). This lends additional credence to our redshift identifications. While each of the literature samples have different measures for q (ranging 1.3–2.2), all with uncertainties on the order of $\sim$0.15–0.25, the overall trend of an evolving q_{IR} is consistent between samples.

4.3. Composite Ultraviolet Spectra

Since the S/N on individual galaxy spectra shown in Figure 3 is quite low for most sources (except in the detection of Lyα), we construct a composite rest-frame ultraviolet spectrum, which can serve two purposes: it validates bulk redshift identification by way of detecting lower S/N spectral features around Lyα and it begins to shed light on the intrinsic rest-frame ultraviolet emission properties of extremely infrared-luminous starbursts. Unfortunately, larger samples are necessary to perform the latter analysis; in this work, our primary goal is to help validate our redshift identifications through cross-correlation to the composite spectrum for sources with only single-line identifications (e.g., Lyα).

It is clear from Figure 3 that these infrared-starbursts exhibit a wide range in spectral properties, from Lyman Break Galaxy (LBG) spectra, quasar spectra, starburst spectra, to those with very steep to very shallow UV slopes. We classify sources as LBGs if they exhibit a steep cutoff in continuum flux at rest-frame 1216 Å, as quasars if they exhibit broad, high-ionization emission lines, and as starbursts for those narrow-emission line galaxies whose emission line luminosity is more significant than continuum luminosity. Many sources are dust obscured and thus are noisy except for the detection of Lyα emission. The construction of a composite spectrum serves as a sanity check on the redshifts. The detection of lower S/N features in a composite spectrum does not *directly* confirm that every galaxy added in is correctly identified, but it does indicate that most of them are. Since co-adding spectra from higher S/N sources would wash out the low S/N features of the other galaxies (in a sample of 36), we exclude the following sources from the composites (excluded on the basis of detection of non-Lyα spectral features at >3σ significance, including continuum and C IV): 1HERMES X24 J033136.96−275510.9, 1HERMES X24 J095917.28+021300.4, 1HERMES X24 J095948.00+024140.7,

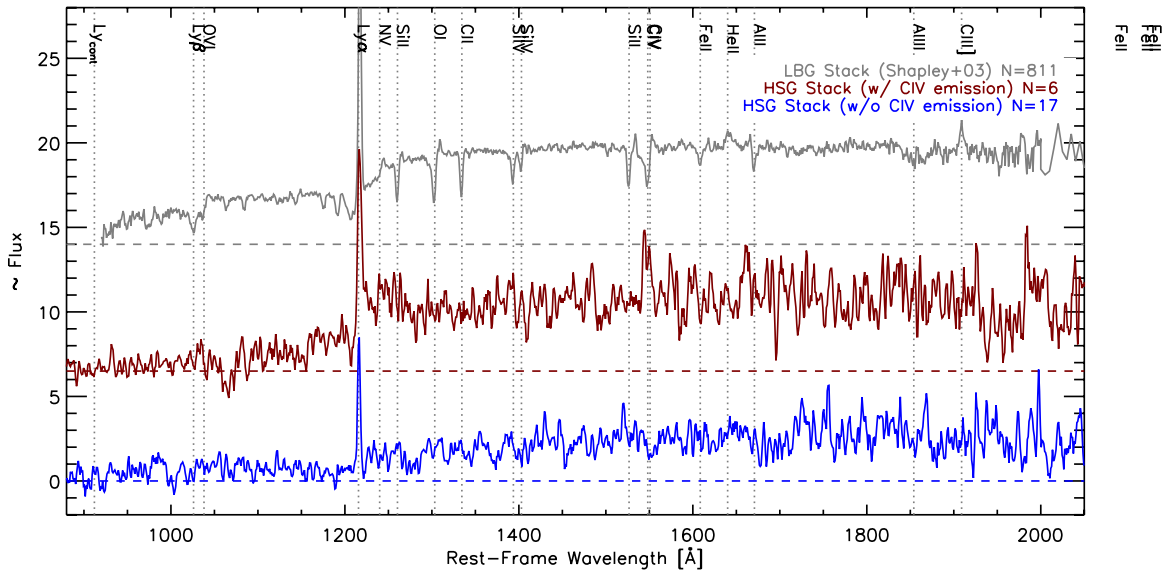

Figure 7. Comparison of the rest-frame ultraviolet composite spectra for *Herschel*-selected galaxies (HSGs) with the composite of Lyman break galaxies (LBGs; top spectrum) compiled in Shapley et al. (2003) from 811 individual galaxies. The composite spectra of HSGs are split into those with C IV emission (middle spectrum) and C IV absorption (bottom spectrum) and *exclude* all sources with high-S/N ($>3\sigma$) spectral features that are not Lyα emission. There are six galaxies in the C IV emission stack and 17 galaxies in the C IV absorption stack, both having a median redshift of $\langle z \rangle = 3.6$. Lyα and the Lyman break, Si IV absorption, and C IV emission/absorption are detected in both composites. More observations of similar sources are needed to enhance the S/N of the composites, which exhibit a wide range of spectral properties (as seen here and in Figure 3). The spectra are arbitrarily offset in flux with marked zero points.

(A color version of this figure is available in the online journal.)

1HERMES X1.4 J100008.64+022043.1, 1HERMES X24 J100020.16+021725.2, 1HERMES X24 J100036.00+021127.6, 1HERMES X1.4 J100024.00+021210.9, 1HERMES X1.4 J100111.52+022841.3, 1HERMES X24 J100146.56+024035.6, 1HERMES X1.4 J104620.40+585933.4, 1HERMES X1.4 J104636.00+585650.0, 1HERMES X24 J160545.99+534544.4, and 1HERMES X1.4 J033151.94−275326.9. In other words, the composite spectra are only made up of Lyα single-line detections, those with low $\sim 2\sigma$–3σ C IV detections, and those without.

Two different composites are constructed based on the detection or non-detection of C IV emission at this low S/N level. Since most starbursts are expected to show absorption in C IV, the co-addition of sources with and without C IV might easily yield a null result and no absorption or emission. Six sources are co-added in the C IV emission composite (these are the remaining sources for which C IV emission is detected, as indicated in Table 1, attributed to an AGN). The remaining 17 sources are co-added to form the composite without C IV emission. Each composite is constructed by scaling the flux of each galaxy to an arbitrary fixed mean value in the wavelength range 1330–1400 Å. This wavelength range is chosen for its proximity to Lyα and absence of spectral signatures. The two composite rest-frame ultraviolet spectra are shown in Figure 7.

Both composites show a very high-S/N Lyα line, a Lyα break, Si IV absorption, and either C IV emission or absorption. The composite LBG spectrum from Shapley et al. (2003) is shown for comparison, although the relative sample sizes should be contrasted. The C IV emission composite, by design, consists of galaxies with non-negligible AGN emission; as a result, the width of the Lyα line is broader in the C IV emission composite than in the C IV absorption composite.

We test for consistency between the composite spectra and individual source spectra through cross-correlation in the off-Lyα wavelength regions (note that for each galaxy's spectrum, we measure the cross-correlation with a composite *excluding* that source). This provides an indication of sources that might be contaminating the composite rather than boosting its S/N. All individual sources in the C IV composite have correlations >0.4 at $\Delta\lambda = 0$ offsets. The individual source spectra making up the other composite are of lower S/N, and have cross-correlations ranging 0.2–0.7. However, four sources (1 HERMES X24 J095830.24+015633.2, 1 HERMES X1.4 J104707.69+585149.1, 1 HERMES X1.4 J104649.92+590039.6, and 1 HERMES X1.4 J123536.28+623019.9) have almost no correlation with the composite (0.05–0.15), which is caused by no continuum detection (since only the off-Lyα spectra are considered in the cross-correlation test). Three of these sources are considered "tentative" in their spectroscopic identifications in Table 1. The fourth source, 1 HERMES X24 J095830.24+015633.2, is secure as judged by the quality of the Lyα detection and the inconsistency of this line being incorrectly identified as [O II].

4.4. Spectral Signatures of AGNs

Since many of the sources in our sample have clear AGN features in their optical spectra, one might think that the infrared luminosities are contaminated by significant AGN heating rather than starburst heating. Typically, the presence of an AGN warms dust to temperatures $\gtrsim$100–200 K. In this sample the majority of galaxies have dust temperatures $\lesssim$70 K. Furthermore, two QSOs and the 13 sources with C IV detections have dust temperatures in the 30–50 K range, perfectly consistent with star formation-dominated infrared emission. While there is still potential for AGN contribution to $L_{\rm IR}$, the lack of correlation with dust temperature indicates that the effect is small ($\lesssim$25%, the nominal contribution of mid-infrared power-law emission to $L_{\rm IR}$; Casey 2012). This is consistent with prior measures of SMGs with AGN ranging $\sim$15%–25% (Swinbank et al. 2004; Pope et al. 2008; Menéndez-Delmestre et al. 2009; Laird et al. 2010; Coppin et al. 2010). Note that one study, Alexander et al. (2005),

could be interpreted to disagree with this work (finding ∼75% of SMGs have AGNs); however, a minority of the sources in that data have AGNs that dominate the sources' bolometric luminosity.

We can draw some basic conclusions from the C IV emission and spectral types in our sample to infer the overall AGN content of $z > 2$ HSGs. For sources of sufficient S/N ($>5\sigma$ in continuum), we can assess AGN spectral signatures source by source. Of the 20 galaxies that meet this S/N cut, there are three LBGs, three quasars, seven starbursts with AGN (e.g., C IV emission), and seven "pure" starbursts (see Table 1 for details). Of the remaining single-line identifications, none show AGN signatures. Of the 36 sources, 10 have AGN signatures, three of which are obvious quasars. Although very qualitative, this analysis implies an AGN fraction of ∼ 25% for the $z > 2$ HSG sample. From the composite spectra (which was constructed from only the lower luminosity sources), our statistics agree by construction; in other words, 6 out of 23 sources had C IV emission, or ∼ 26%. In a series of detailed studies on the multiwavelength properties of 850 μm selected SMGs, Alexander et al. (2005), Pope et al. (2008), and Menéndez-Delmestre et al. (2009) also measure AGN fractions ≈25% for similarly luminous $z \sim 2$ starbursts.

Interestingly, the sources exhibiting AGN signatures in the optical do not show hotter dust temperature SEDs in the infrared. One might expect higher dust temperatures in the infrared with the presence of an AGN heating the surrounding material to temperatures ∼100–200 K, exceeding normal heating from star formation, ∼30–50 K. The sources with AGN signatures are marked with small white dots in Figure 5. The observation that the AGN does not seem to have a significant impact on infrared luminosity or dust temperature is not surprising if you consider that the star formation activity is at least an order of magnitude more luminous.

Although the selections of the SMG population and the HSG population differ, finding 1/4 with AGN might suggest that HSGs are similar in most ways to SMGs without any enhanced AGN activity, despite slightly warmer overall dust temperatures and brighter mid-infrared fluxes in comparison (described in the next section). However, further detailed work on these samples is needed before any conclusion is drawn as to the evolutionary nature of these *Herschel*-selected galaxies relative to classic 850 μm selected SMGs.

4.5. Composite Infrared Spectra

Figure 8 combines all SPIRE, *Spitzer*, and PACS (where available) infrared photometry for all galaxies in our sample from rest-frame ≈ 40–150 μm and radio data. This includes observations at 24 μm, 70 μm, 100 μm, 160 μm, 250 μm, 350 μm, and 500 μm. At these redshifts, the SPIRE bands probe the Wien-side of the thermal dust emission peak. Mean SEDs are fit using the modified blackbody plus power-law method described by Equation (1) for photometric data that are scaled to the mean infrared luminosity of the sample, $\langle L_{\rm IR}\rangle = 1.8 \times 10^{13}\ L_{\odot}$, and then separately, scaled to the mean radio flux density of the sample, $\langle S_{1.4}\rangle = 95\ \mu$Jy (or rest-frame $S_{1.4} = 283\ \mu$Jy assuming $\alpha = 0.75$). While all 36 galaxies are used in the former SED fit (top panel of Figure 8), the radio-scaled SED fit only has contributions from radio-detected galaxies.

There are two notable aspects of these mean SED fits seen in Figure 8; the first is the difference between the observed 24 μm flux densities relative to predictions from an 850 μm selected SMG template spectrum (Pope et al. 2008), and the second

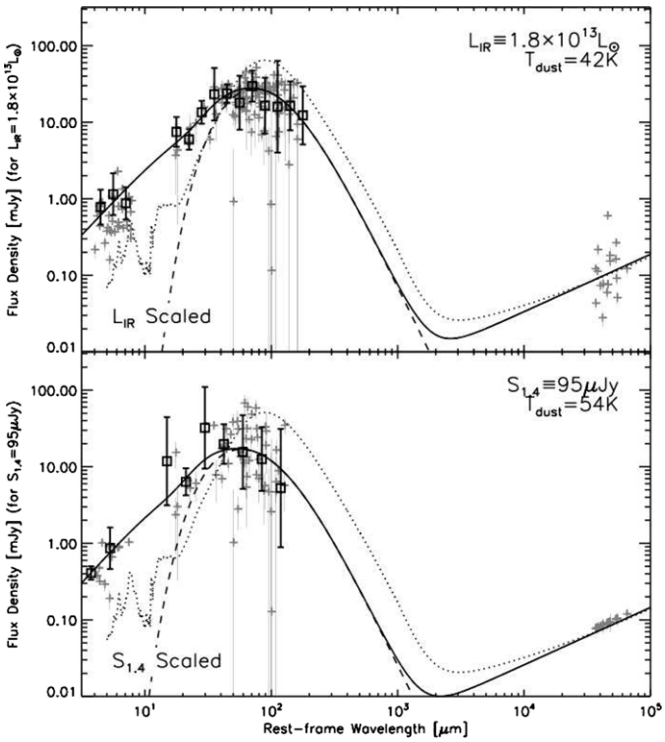

Figure 8. Mean infrared and radio SEDs for the sample re-normalized to the mean IR luminosity of the sample, $1.8 \times 10^{13}\ L_{\odot}$ (top), and to mean radio flux density, 95 μJy (bottom). The mean normalized flux density in $\log(\lambda) = 0.1$ bins is shown as black squares, from rest-frame ≈4–150 μm. Best-fit SEDs (solid black lines) are generated as described in the text according to Equation (1) with fixed $\beta = 1.5$. They comprise a cold-dust-modified blackbody fit (dashed line) and a mid-infrared power-law representative of warm dust emission. Radio synchrotron emission is added onto this best-fit infrared SED by assuming the FIR/radio correlation holds with a synchrotron slope of $\alpha = 0.75$. The composite SMG SED described in Pope et al. (2008) is shown as a dashed line. Both the luminosity-scaled SED and radio-scaled SED appear to have a 24 μm excess relative to the SMG expectation. The radio-scaled SED has a hotter characteristic dust temperature than the luminosity-scaled SED (both of which are uncertain by ∼3 K), likely driven by the bias against colder-dust galaxies of similar flux densities (less likely to be radio detected).

is the difference in dust temperatures between luminosity- and radio-scaled SEDs. The issue of the discrepancy of mid-infrared emission relates to the ongoing discussion of suppression of polycyclic aromatic hydrocarbon (PAH) emission in infrared starburst galaxies (e.g., Elbaz et al. 2011), where it is suggested that most normal galaxies have a fixed ratio (≡IR8) between 7.7 μm emission (or ≈8 μm emission) and total integrated infrared luminosity $L_{\rm IR}$ and that sources with enhanced infrared emission are called infrared starbursts. However, as Hainline et al. (2009) point out, the mid-infrared portion of the spectrum does not lend itself to simple interpretation in terms of what is or is not AGN dominated or starburst dominated. SMGs, known to be extreme starbursts, do in fact have enhanced infrared emission relative to PAH strength (e.g., see Pope et al. 2008; Menéndez-Delmestre et al. 2009), however in this sample—which is on average more distant than most 850 μm selected SMGs—we see mid-infrared flux densities ∼2–5 times the SMG expectation, more consistent with the measured IR8 value for most "main-sequence" galaxies. What does this suggest about the SPIRE sample's evolutionary histories? Is PAH emission simply not suppressed in these distant starbursts, or could the 24 μm "excess" be due to AGN heating? Or could these high-redshift infrared-luminous galaxies be "main-sequence" secularly evolving galaxies? While this might be a

selection bias based on 24 μm or 1.4 GHz detectability, the radio-selected galaxies (bottom panel) still show a mid-infrared excess above expectation from the SMG template.

The differences in dust temperatures between the two mean SED fits (42 ± 3 K versus 54 ± 4 K for luminosity-scaled and radio-scaled, respectively) is traceable to a radio selection bias. For two galaxies with similar Spire flux densities, one with a warm temperature ($\sim$60 K) and one with a cold temperature ($\sim$30 K), the galaxy with the warm temperature is going to have a much higher integrated infrared luminosity and therefore much brighter 1.4 GHz detection at these redshifts. Therefore, when we consider just radio-detected galaxies, the average dust temperature increases due to the exclusion of cold, non-detectable galaxies.

As discussed earlier, we estimate that 16%–43% of these galaxies would be formally undetected at 850 μm at $<$ 2–5 mJy. In other words, 16%–43% of HSGs at $z > 2$ are consistent with the submillimeter faint radio galaxy (SFRG, formerly optically faint, "OFRG") selection and not SMG selection (Chapman et al. 2004a, 2010; Magdis et al. 2010; Casey et al. 2009, 2011a, 2011b). The composite infrared SEDs from Figure 8 support this conclusion, since the range of observed 850 μm flux densities from the best-fit SEDs is in the 1 mJy $< S_{850} <$ 10 mJy range, not as luminous at long wavelengths as the 850 μm selected composite (Pope et al. 2008).

5. SFRD IMPLICATIONS AND DISCUSSION

To place these $z > 2$ Spire-selected galaxies in context with other high-z infrared galaxies and lower luminosity galaxies, we estimate their contribution to the cosmic SFRD (Madau et al. 1996, 1998; Hopkins & Beacom 2006). The SFRD contribution allows a direct comparison of the importance of infrared-luminous galaxies to the buildup of stellar mass in the universe over a range of epochs. At lower redshifts $z \lesssim 1$, ULIRGs are very rare and contribute little to the SFRD (Sanders et al. 2003), but toward $z \approx 1$ the importance of ULIRGs grows, and it is estimated that LIRGs and ULIRGs ($L_{\rm IR} > 10^{11}$ $L_\odot$) could contribute as much as $\sim$1/2 of the total SFRD (see results from *Spitzer*; Le Floc'h et al. 2005, and work in C12). At $z > 1$, the contribution of infrared-luminous sources is much more difficult to measure, limited by small numbers of SMGs (Chapman et al. 2005; Wardlow et al. 2011) or complex selection biases or extrapolations from the mid-infrared (Caputi et al. 2007; Magnelli et al. 2011; Capak et al. 2011). The $2 < z < 5$ galaxies in this paper provide a unique sample to make this measurement, due to their well-characterized selection over a relatively large sky area, $\sim$1 deg^2.

To arrive at SFRD estimates, we first compute the infrared luminosity function using a $1/V_{\rm max}$ method, where each source is associated with the maximum volume in which it could be detected at its given luminosity, $L_{\rm IR}$ (Schmidt 1968). The number density of sources with luminosity between L and $L + \Delta L$ is given as $\Phi_z(L)\Delta L = \sum 1/(V_i(L) \times c_i)$ in units of h^3 Mpc^{-3} log L^{-1}. Here c_i is a completeness estimator that corrects for sample incompleteness at the selection wavelength, e.g., in this case, at 250–500 μm. C12 presents a detailed discussion of this completeness factor as a function of selection wavelength flux density, which varies field to field (based on the prior source catalog depths). Sources with flux densities $>$15 mJy will be more than 90% complete (e.g., $c_i > 0.9$) in all fields.

The completeness estimator's effect on the integrated SFRD is small compared with the uncertainty in the luminosity function itself from small number counts. Note, however, that this correction only pertains to one of the many sources of incompleteness of this sample; it is far more difficult to quantify and correct for incompleteness with respect to sources missing from the prior catalog list (e.g., 1.4 GHz or 24 μm faint), which is particularly a problem at $z > 2$, as well as spectroscopic incompleteness, i.e., the galaxies that have no detectable emission lines or are too optically obscured to be identified.

$V_i(L)$ is the maximum volume in which source i could reside and still be detectable by our survey. Since the detection limits of Spire alter between field catalogs, the detection limit determining the maximum volume is calculated source by source. This luminosity detection limit is determined much like the curves in Figure 6. For example, a source might have its highest S/N at 350 μm, then its luminosity detection limit, thus maximal redshift limit $z_{\rm max}$, is determined by setting a 3σ detection threshold at 350 μm where sigma is the local confusion plus instrumental noise in the 350 μm map. This $z_{\rm max}$ limit is then found across the entire survey area probed to determine accessible volume. The assumed dust temperature is that measured for the given source (since dust temperature does impact the steepness of the luminosity limit with redshift).

We split the luminosity function into two redshift bins: $2.0 < z < 3.2$ and $3.2 < z < 5.0$ with 15 sources in the former and 20 in the latter. Since LRIS and DEIMOS have different wavelength coverage, DEIMOS observations suffer from a redshift desert from $1.6 < z < 3.2$ that LRIS observations do not, so we split the sample at $z = 3.2$ and only compute the density using LRIS observations between $z = 2.0$ and $z = 3.2$. This excludes two sources from the calculation (1HERMES X1.4 J104636.00+585650.0 at $z = 2.841$ and 1HERMES X24 J160545.99+534544.4 at $z = 2.555$) that were both surveyed with DEIMOS and detected in the redshift desert due to strong C IV emission caused by the presence of a quasar. Since high-redshift $z \gtrsim 2$ sources are only detectable on the masks observed in the best weather conditions, the effective area probed by LRIS for this calculation is 0.13 deg^2 over the range $2.0 < z < 5.0$ and for DEIMOS 0.30 deg^2 over the range $3.2 < z < 5.0$. The resulting *spectroscopically incomplete* luminosity functions are shown in Figure 9.

Since some of our identifications are less confident than others (e.g., those marked with a † in Table 1), we also compute the luminosity function excluding tentative identifications. The result is seen in Figure 9: while the $2.0 < z < 3.2$ luminosity function remains the same (differing only by two sources), the $3.2 < z < 5.0$ luminosity function drops by 11 sources (salmon versus dark red luminosity functions).

The SFRD is then the luminosity-weighted integral of the luminosity function, or the raw summation of the luminosity (converted to SFR) over accessible volume: $(7.0 \pm 2.0) \times 10^{-3}$ $M_\odot$ yr^{-1} h^3 Mpc^{-3} at $2.0 < z < 3.2$ and $(5.5 \pm 0.6) \times 10^{-3}$ $M_\odot$ yr^{-1} h^3 Mpc^{-3} at $3.2 < z < 5.0$ (full sample) and $(2^{+3}_{-1}) \times 10^{-3}$ $M_\odot$ yr^{-1} h^3 Mpc^{-3} at $3.2 < z < 5.0$ (high confidence sample), shown in Figure 10 against other comparison populations. These points are lower limits since they do not include any sources that might be excluded from the prior catalogs at 24 μm or 1.4 GHz, which is speculated to be a non-negligible fraction ($\gtrsim$20%) at $z > 2$ (e.g., Magdis et al. 2010; I. Smail et al. 2012, in preparation). Note also that the luminosity limits of the two redshift bins differ: the $z \sim 2.5$ bin covers $10^{12.4}$–$10^{13.2}$ $L_\odot$ while the $z \sim 4$ bin covers $10^{12.8}$–$10^{13.6}$ $L_\odot$. To assess luminosity evolution from $z \sim$ 2–5, we compute the SFRD contributions in the overlapping luminosity range of

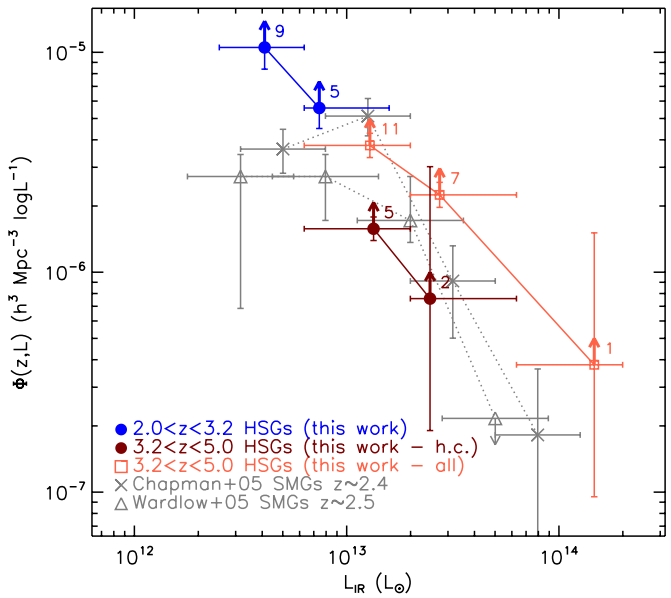

Figure 9. Estimated luminosity function for $2 < z < 5$ *Herschel*-SPIRE-selected galaxies compared to the luminosity function of 850 μm selected SMGs at $z \approx 2.5$ (Chapman et al. 2005; Wardlow et al. 2011). Up arrows denote the fact that this survey is *spectroscopically incomplete* and that the incompleteness is not well quantified at $z > 2$. Numbers next to each point indicate how many galaxies from our sample contribute to that luminosity bin; the numbers are comparable to those in the $z \approx 2$ SMG samples. The luminosity function for the whole sample at $3.2 < z < 5.0$ is shown in salmon, while the high confidence (h.c.) identifications' luminosity function is shown in dark red.

(A color version of this figure is available in the online journal.)

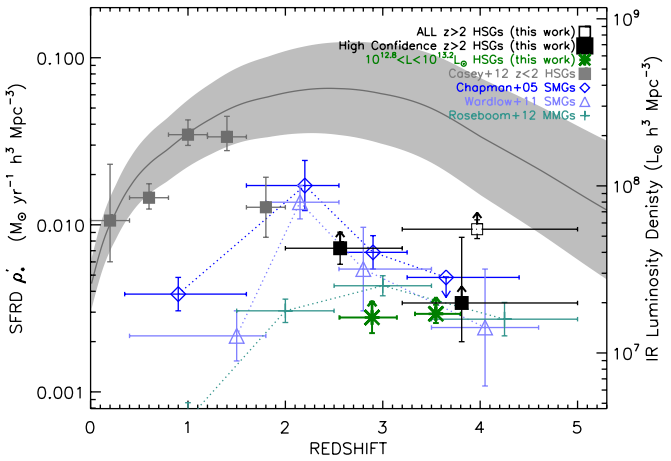

Figure 10. Star formation rate density of *Herschel*-SPIRE-selected galaxies (black points) relative to 850 μm selected SMGs (Chapman et al. 2005; Wardlow et al. 2011) and 1.2 mm selected MMGs (Roseboom et al. 2012). The compilation of SFRD measurements from Hopkins & Beacom (2006) is shown as a gray band, which is largely drawn from optical or rest-frame ultraviolet-selected galaxy populations corrected for dust extinction. The luminosity limits of integration are $10^{12.4}$–$10^{13.4}$ $L_\odot$ at $z \sim 2.5$ and $10^{12.8}$–$10^{13.6}$ $L_\odot$ at $z \sim 4$; the SFRD from sources sitting in the luminosity where the two redshift bins overlap ($10^{12.8}$–$10^{13.2}$ $L_\odot$) is shown in green. The SFRD measurements for *Herschel*-selected galaxies at $z < 2$ are shown as gray points. The sharp drop in the SFRD of *Herschel*-selected samples at $z \sim 2$ is caused by the redshifting of the SED peak such that more infrared-luminous galaxies are SPIRE "dropouts" and that only the warmest, most luminous $>10^{13}$ $L_\odot$ systems are detectable with SPIRE at $z > 2$. Note that we observe an increase in the infrared-luminous contribution to the SFRD from $z \sim 2.6$ to $z \sim 4$.

(A color version of this figure is available in the online journal.)

both redshift bins, $10^{12.8}$–$10^{13.2}$ $L_\odot$, shown as green points in Figure 10.

Although these measurements of the *Herschel* contribution to the SFRD at $2 < z < 5$ are lower limits due to our survey's incompleteness, the effects of gravitational lensing and clustering could lead to an overestimation. Are these effects significant in this sample? For the former we use the conditional lensing probability as a function of SPIRE flux density (F. De Bernardis 2011, private communication; Wardlow et al. 2012). For SPIRE flux densities $S_{500} < 80$ mJy, the distribution in number counts is dominated by a Schechter function rather than the flat-sloped source counts at > 80 mJy; galaxies with $S_{500} > 80$ mJy have a high probability of being lensed by factors > 2, while this model predicts a mean lensing factor for this sample of $\langle\mu\rangle < 1.05$, which changes negligibly between $z = 2$ and $z = 5$.

The brightest source in our sample with $S_{250} = 73.1$ mJy, 1HERMES X24 J161506.65+543846.9, has the highest probability of being lensed (its expected lensing factor is $\langle\mu\rangle = 1.2$). It is the highest redshift source in our sample at $z = 4.952$. Due to its extreme luminosity compared with the rest of the sample and its tentative spectroscopic identification, we exclude this source from the SFRD measurement.

To assess the impact of clustering on the SFRD measurement, we need a good grasp of the spatial density of $z > 2$ sources on our slit masks and the possibility of biased placement of slit masks around high-z clusters. The former can be gauged by the number of high-z confirmations per slit mask; the 36 sources of this sample are distributed across 12 LRIS masks and 14 DEIMOS masks, with an additional 5 LRIS masks and 3 DEIMOS masks without any high-z sources; this averages to 0–2 galaxies per mask without any mask having more than 2 sources. Since the masks were distributed randomly with respect to one another in each field and none of the masks were close together, this demonstrates that these sources are indeed randomly distributed over the surveyed area, 0.93 deg^2 for the whole survey.

The possibility exists that there is an intrinsic bias of the placement of our slit-masks such that more high-z sources are observed than elsewhere. As explained in detail in C12, masks were placed around high-priority targets, which were "red" in their SPIRE colors (e.g., $S_{250} < S_{350} < S_{500}$ all with $S \gtrsim 15$ mJy) and thought to be high-redshift sources. Of the 36 confirmed $z > 2$ sources, seven (~19%) were originally high-priority targets. However, an additional 44 high-priority targets were identified at $z < 2$ and 78 were unidentified. Relative to the number of high-priority sources targeted, we measure $5\% \pm 5\%$ as identified at $z > 2$, $34\% \pm 5\%$ at $z < 2$ and $60\% \pm 4\%$ unidentified. The same statistics for lower priority targets are $2\% \pm 1\%$ at $z > 2$, $48\% \pm 1\%$ at $z < 2$, and $50\% \pm 1\%$ unidentified. Within uncertainties, the proportion of sources identified at $z > 2$ are the same between low-priority and high-priority targets, indicating no bias or advantage in targeting "red" sources more than any other significant *Herschel*-SPIRE source. This implies that no clustering correction on the measured SFRD is necessary.

The lower limits to the SFRD set by SPIRE sources tells us that the early universe potentially had a very substantial amount of star formation in short-lived, intense >1000 $M_\odot$ yr^{-1} bursts as opposed to slow-progressing moderate levels of star formation. The contribution from SPIRE to the SFRD at these epochs is at least comparable to the contribution measured from longer wavelength-selected galaxies, like the 850 μm selected SMGs (Chapman et al. 2005; Wardlow et al. 2011) or 1.2 mm selected

millimeter galaxies (MMGs; Roseboom et al. 2012). This is made more interesting by the observation that the populations (SMG and HSG) only overlap by 21 out of 36 galaxies (58%). Further work aimed at confirming redshifts of $z > 2$ Spire sources, particularly those without radio or 24 μm counterparts, is needed to constrain these lower limits into real measurements so the importance of $\gtrsim 10^{13}$ $L_\odot$ activity in the first few Gyr of the universe is understood.

6. CONCLUSIONS

The identification of SMGs at early epochs in the universe's history is the key to understanding the limits of star formation and galaxy evolution on short timescales. This paper has presented new observations of 36 *Herschel*-Spire-selected starburst galaxies between $2 < z < 5$, taken from a large Keck spectroscopic survey of 1594 Spire-selected galaxies covering 0.93 deg^2.

We present the following conclusions.

1. Our sample of 36HSGs constitute some of the brightest, most extreme infrared starburst galaxies in the universe. Spanning $2 < z < 5$, our sample has a mean luminosity $\langle L_{\rm IR} \rangle = 1.8 \times 10^{13}\ L_\odot$ (SFR $\approx 3100\ M_\odot\ {\rm yr}^{-1}$).
2. These $2 < z < 5$ HSGs have a well-characterized selection across six legacy fields and 0.93 deg^2; galaxies must be $>3\sigma$ significant in one of the three *Herschel*-Spire bands and also be detected in deep 24 μm and/or 1.4 GHz survey coverage. Although it misses 24 μm or 1.4 GHz high-z dropouts, the selection is identical to low-z HSG selection. Sources at $z > 2$ comprise 5% of all galaxies selected via this method; although inefficient for finding high-z infrared galaxies, the selection is easily reproducible and well suited for volume density estimates.
3. Our sample show a wide range of rest-frame ultraviolet spectral features: some galaxies classifiable as quasars, some as LBGs, and most as starbursts with a wide range of dust extinctions/reddening. The heterogeneous nature of their spectra provides additional evidence that the infrared-luminous stage might exist during a period when the host galaxy is rapidly evolving.
4. The radio-detected subset of our sample (23/36) follow the FIR/radio correlation consistent with moderate evolution in $q_{\rm IR}$ from previous work (Ivison et al. 2010b).
5. We construct composite rest-frame ultraviolet spectra and rest-frame infrared SEDs to assess some aggregate properties of HSGs. In the rest-frame UV, we determine that 25% of HSGs exhibit C IV emission (a signature of AGN). In the infrared, HSGs exhibit a 24 μm excess relative to SMGs of similar $L_{\rm IR}$; without mid-IR spectra, it is impossible to know whether this is due to enhanced PAH emission (similar to "normal" galaxies) or AGN emission. The dust temperatures of radio-selected samples are warmer than those of the full sample.
6. Our spectroscopic survey is incomplete due to selection bias at 24 μm and 1.4 GHz, as well as spectroscopic incompleteness caused by heavy dust obscuration in the rest-frame UV. Therefore, we are able to place *lower limits* on the contribution of $2 < z < 5$ HSGs to the cosmic SFRD, which is $>7 \times 10^{-3}\ M_\odot\ {\rm yr}^{-1}\ h^3\ {\rm Mpc}^{-3}$ at $z \approx 2.6$ and $>3 \times 10^{-3}\ M_\odot\ {\rm yr}^{-1}\ h^3\ {\rm Mpc}^{-3}$ at $z \approx 4$, corresponding to >10% and >20% of the best estimates of the total SFRD at their respective epochs.

This work highlights the importance of extremely luminous FIR-bright galaxies to the buildup of stellar mass, particularly at early times in the universe's history. Further work on constraining completeness and the parent population of infrared-luminous galaxies at $z > 2$ is needed to understand the role that short-lived starbursts have in the context of galaxy evolution and formation.

C.M.C. is generously supported by a Hubble Fellowship from Space Telescope Science Institute, grant HST-HF-51268.01-A. The data presented herein were obtained at the W. M. Keck Observatory, which is operated as a scientific partnership among the California Institute of Technology, the University of California, and the National Aeronautics and Space Administration. The Observatory was made possible by the generous financial support of the W. M. Keck Foundation. The authors recognize and acknowledge the very significant cultural role and reverence that the summit of Mauna Kea has always had within the indigenous Hawaiian community. We are most fortunate to have the opportunity to conduct observations from this mountain. This work would not be possible without the hard work and dedication of the Keck Observatory night and day staff; special thanks to Marc Kassis, Luca Rizzi, and Greg Wirth for help and advice while observing. The analysis pipeline used to reduce the DEIMOS data was developed at UC Berkeley with support from NSF grant AST-0071048.

Spire has been developed by a consortium of institutes led by Cardiff Univ. (UK) and including: Univ. Lethbridge (Canada); NAOC (China); CEA, LAM (France); IFSI and Univ. Padua (Italy); IAC (Spain); Stockholm Observatory (Sweden); Imperial College London, RAL, UCL-MSSL, UKATC, and Univ. Sussex (UK); and Caltech, JPL, NHSC, and Univ. Colorado (USA). This development has been supported by national funding agencies: CSA (Canada); NAOC (China); CEA, CNES, CNRS (France); ASI (Italy); MCINN (Spain); SNSB (Sweden); STFC, UKSA (UK); and NASA (USA).

This research has made use of data from the HerMES project (http://hermes.sussex.ac.uk/). HerMES is a *Herschel* Key Programme utilizing Guaranteed Time from the Spire instrument team, ESAC scientists, and a mission scientist. HerMES is described in Oliver et al. (2012). The Spire data presented in this paper will be released through the HerMES Database in Marseille, HeDaM (http://hedam.oamp.fr/HerMES).

REFERENCES

Alexander, D. M., Bauer, F. E., Chapman, S. C., et al. 2005, ApJ, 632, 736
Barger, A. J., Cowie, L. L., Sanders, D. B., et al. 1998, Nature, 394, 248
Béthermin, M., Dole, H., Lagache, G., Le Borgne, D., & Penin, A. 2011, A&A, 529, A4
Biggs, A. D., & Ivison, R. J. 2008, MNRAS, 385, 893
Blain, A. W., Barnard, V. E., & Chapman, S. C. 2003, MNRAS, 338, 733
Blain, A. W., Chapman, S. C., Smail, I., & Ivison, R. 2004, ApJ, 611, 725
Blain, A. W., Smail, I., Ivison, R. J., Kneib, J., & Frayer, D. T. 2002, Phys. Rep., 369, 111
Bridge, C. R., Blain, A., Borys, C. J. K., et al. 2012, arXiv:1205.4030
Capak, P. L., Riechers, D., Scoville, N. Z., et al. 2011, Nature, 470, 233
Caputi, K. I., Lagache, G., Yan, L., et al. 2007, ApJ, 660, 97
Cardamone, C. N., van Dokkum, P. G., Urry, C. M., et al. 2010, ApJS, 189, 270
Casey, C. M. 2012, MNRAS, 425, 3094
Casey, C. M., Chapman, S. C., Beswick, R. J., et al. 2009, MNRAS, 399, 121
Casey, C. M., Chapman, S. C., Neri, R., et al. 2011a, MNRAS, 415, 2723
Casey, C. M., Chapman, S. C., Smail, I., et al. 2011b, MNRAS, 411, 2739
Casey, C. M., Béthermin, M., Bock, J., et al. 2012, ApJ, 761, 140
Chapin, E. L., Chapman, S. C., Coppin, K. E., et al. 2011, MNRAS, 411, 505
Chapman, S. C., Blain, A. W., Smail, I., & Ivison, R. J. 2005, ApJ, 622, 772
Chapman, S. C., Helou, G., Lewis, G. F., & Dale, D. A. 2003, ApJ, 588, 186

Chapman, S. C., Ivison, R. J., Roseboom, I. G., et al. 2010, MNRAS, 409, L13
Chapman, S. C., Smail, I., Blain, A. W., & Ivison, R. J. 2004a, ApJ, 614, 671
Chapman, S. C., Smail, I., Windhorst, R., Muxlow, T., & Ivison, R. J. 2004b, ApJ, 611, 732
Chary, R., & Elbaz, D. 2001, ApJ, 556, 562
Clements, D. L., Vaccari, M., Babbedge, T., et al. 2008, MNRAS, 387, 247
Condon, J. J. 1992, ARA&A, 30, 575
Conley, A., Cooray, A., Vieira, J. D., et al. 2011, ApJ, 732, L35
Coppin, K., Pope, A., Menéndez-Delmestre, K., et al. 2010, ApJ, 713, 503
Coppin, K. E. K., Smail, I., Alexander, D. M., et al. 2009, MNRAS, 395, 1905
Cowie, L. L., Songaila, A., Hu, E. M., & Cohen, J. G. 1996, AJ, 112, 839
Cox, P., Krips, M., Neri, R., et al. 2011, ApJ, 740, 63
Daddi, E., Dannerbauer, H., Stern, D., et al. 2009, ApJ, 694, 1517
Dale, D. A., & Helou, G. 2002, ApJ, 576, 159
Davé, R., Finlator, K., Oppenheimer, B. D., et al. 2010, MNRAS, 404, 1355
Dekel, A., Birnboim, Y., Engel, G., et al. 2009, Nature, 457, 451
Draine, B. T., & Li, A. 2007, ApJ, 657, 810
Eales, S., Lilly, S., Gear, W., et al. 1999, ApJ, 515, 518
Elbaz, D., Dickinson, M., Hwang, H. S., et al. 2011, A&A, 533, A119
Griffin, M. J., Abergel, A., Abreu, A., et al. 2010, A&A, 518, L3
Hainline, L. J., Blain, A. W., Smail, I., et al. 2009, ApJ, 699, 1610
Helou, G., Soifer, B. T., & Rowan-Robinson, M. 1985, ApJ, 298, L7
Hinshaw, G., Weiland, J. L., Hill, R. S., et al. 2009, ApJS, 180, 225
Hopkins, A. M., & Beacom, J. F. 2006, ApJ, 651, 142
Hughes, D. H., Serjeant, S., Dunlop, J., et al. 1998, Nature, 394, 241
Ibar, E., Ivison, R. J., Best, P. N., et al. 2010, MNRAS, 401, L53
Ilbert, O., Salvato, M., Le Floc'h, E., et al. 2010, ApJ, 709, 644
Ivison, R. J., Alexander, D. M., Biggs, A. D., et al. 2010a, MNRAS, 402, 245
Ivison, R. J., Chapman, S. C., Faber, S. M., et al. 2007, ApJ, 660, L77
Ivison, R. J., Magnelli, B., Ibar, E., et al. 2010b, A&A, 518, L31
Kennicutt, R. C., Jr. 1998, ApJ, 498, 541
Kovács, A., Omont, A., Beelen, A., et al. 2010, ApJ, 717, 29
Laird, E. S., Nandra, K., Pope, A., & Scott, D. 2010, MNRAS, 401, 2763
Le Floc'h, E., Aussel, H., Ilbert, O., et al. 2009, ApJ, 703, 222
Le Floc'h, E., Papovich, C., Dole, H., et al. 2005, ApJ, 632, 169
Levenson, L., Marsden, G., Zemcov, M., et al. 2010, MNRAS, 409, 83
Lutz, D., et al. 2011, A&A, 532, 90
Madau, P., Ferguson, H. C., Dickinson, M. E., et al. 1996, MNRAS, 283, 1388
Madau, P., Pozzetti, L., & Dickinson, M. 1998, ApJ, 498, 106
Magdis, G. E., Elbaz, D., Hwang, H. S., et al. 2010, MNRAS, 409, 22
Magnelli, B., Elbaz, D., Chary, R. R., et al. 2011, A&A, 528, A35
Magnelli, B., Lutz, D., Santini, P., et al. 2012, A&A, 539, 155
Menéndez-Delmestre, K., Blain, A. W., Smail, I., et al. 2009, ApJ, 699, 667
Mobasher, B., Capak, P., Scoville, N. Z., et al. 2007, ApJS, 172, 117
Neufeld, D. A. 1991, ApJ, 370, L85
Nguyen, H. T., Schulz, B., Levenson, L., et al. 2010, A&A, 518, L5
Oliver, S. J., Bock, J., Altieri, B., et al. 2012, MNRAS, 424, 1614
Pilbratt, G. L., Riedinger, J. R., Passvogel, T., et al. 2010, A&A, 518, L1
Pope, A., Bussmann, R. S., Dey, A., et al. 2008, ApJ, 689, 127
Roseboom, I. G., Ivison, R. J., Greve, T. R., et al. 2012, MNRAS, 419, 2758
Roseboom, I. G., Oliver, S. J., Kunz, M., et al. 2010, MNRAS, 409, 48
Rowan-Robinson, M. 2000, MNRAS, 316, 885
Rowan-Robinson, M., Babbedge, T., Oliver, S., et al. 2008, MNRAS, 386, 697
Sanders, D. B., Mazzarella, J. M., Kim, D.-C., Surace, J. A., & Soifer, B. T. 2003, AJ, 126, 1607
Sanders, D. B., & Mirabel, I. F. 1996, ARA&A, 34, 749
Sanders, D. B., Soifer, B. T., Elias, J. H., et al. 1988, ApJ, 325, 74
Scarlata, C., Colbert, J., Teplitz, H. I., et al. 2009, ApJ, 704, L98
Schmidt, M. 1968, ApJ, 151, 393
Shapley, A. E., Steidel, C. C., Pettini, M., & Adelberger, K. L. 2003, ApJ, 588, 65
Siana, B., Teplitz, H. I., Colbert, J., et al. 2007, ApJ, 668, 62
Siana, B., Teplitz, H. I., Ferguson, H. C., et al. 2010, ApJ, 723, 241
Siebenmorgen, R., & Krügel, E. 2007, A&A, 461, 445
Smail, I., Ivison, R. J., & Blain, A. W. 1997, ApJ, 490, L5
Smolčić, V., Capak, P., Ilbert, O., et al. 2011, ApJ, 731, L27
Strazzullo, V., Pannella, M., Owen, F. N., et al. 2010, ApJ, 714, 1305
Swinbank, A. M., Lacey, C. G., Smail, I., et al. 2008, MNRAS, 391, 420
Swinbank, A. M., Smail, I., Chapman, S. C., et al. 2004, ApJ, 617, 64
Tacconi, L. J., Genzel, R., Smail, I., et al. 2008, ApJ, 680, 246
Walter, F., Decarli, R., Carilli, C., et al. 2012, Nature, 486, 233
Wang, W.-H., Barger, A. J., & Cowie, L. L. 2009, ApJ, 690, 319
Wang, W.-H., Cowie, L. L., Barger, A. J., & Williams, J. P. 2011, ApJ, 726, L18
Wang, W.-H., Cowie, L. L., van Saders, J., Barger, A. J., & Williams, J. P. 2007, ApJ, 670, L89
Wardlow, J. L., Cooray, A., De Bernardis, F., et al. 2012, arXiv:1205.3778
Wardlow, J. L., Smail, I., Coppin, K. E. K., et al. 2011, MNRAS, 415, 1479
Younger, J. D., Omont, A., Fiolet, N., et al. 2009, MNRAS, 394, 1685